

VANADIUM- AND CHROMIUM-BEARING PINK PYROPE GARNET: CHARACTERIZATION AND QUANTITATIVE COLORIMETRIC ANALYSIS

Ziyin Sun, Aaron C. Palke, and Nathan Renfro

A type of pink pyrope garnet containing vanadium and chromium, believed to have been mined in Tanzania, appeared at the 2015 Tucson shows. The material shows a noticeable color difference from purplish pink under incandescent light (A) to purple under daylight-equivalent light (D65). This study reports a quantitative analysis of the difference in color between the two lighting conditions, based on the use of high-quality visible absorption spectroscopy to calculate CIELAB 1976 colorimetric coordinates. L^* , a^* , and b^* colorimetric parameters were calculated for a wide range of path lengths as extrapolated from visible absorption spectra of thinner samples. Using this method, the path length of light through the stone that produces the optimal color difference can be calculated. This path length can then be used to determine the optimal depth range to maximize color change for a round brilliant of a specific material. The pink pyrope studied here can be designated as “color-change” garnet according to certain classification schemes proposed by other researchers. In many of these schemes, however, the material fails to exceed the minimum requirements for quantitative color difference and hue angle difference to be described as “color-change.” Nonetheless, there is no simple solution to the problem of applying color coordinates to classify color-change phenomena. Also presented is a method by which spectra can be corrected for reflection loss and accurately extrapolated to stones with various path lengths.

Garnets are a group of isometric nesosilicates with the general chemical formula $X_3Y_2Z_3O_{12}$. X, Y, and Z represent dodecahedral, octahedral, and tetrahedral sites in the crystal structure, respectively. Natural rock-forming silicate garnets with the Z-site occupied by Si^{4+} are commonly divided into the pyrope and ugrandite groups. In pyrope, Al^{3+} occupies the Y-site and the X-site may contain Mg^{2+} , Fe^{2+} , or Mn^{2+} ; these garnets are dominantly composed of the pyrope ($Mg_3Al_2Si_3O_{12}$), almandine ($Fe^{2+}_3Al_2Si_3O_{12}$), and spessartine ($Mn_3Al_2Si_3O_{12}$) end members. The ugrandite garnets have Ca^{2+} on the X-site and Cr^{3+} , Al^{3+} ,

or Fe^{3+} on the Y-site, giving uvarovite ($Ca_3Cr_2Si_3O_{12}$), grossular ($Ca_3Al_2Si_3O_{12}$), or andradite ($Ca_3Fe^{3+}_2Si_3O_{12}$) end members. Stockton and Manson (1985) proposed a classification scheme for separating the pyrope group into the gemological species of pyrope, almandine, spessartine, pyrope-almandine, pyrope-spessartine, and almandine-spessartine. Previously, two types of color-change garnets have been reported: pyrope with very high Cr^{3+} (Hysingjord, 1971; Carstens, 1973; Amthauer, 1975) and pyrope-spessartine containing both Cr^{3+} and V^{3+} (Crowningshield, 1970; Jobbins et al., 1975; Schmetzer and Ottemann, 1979; Manson and Stockton, 1984; Johnson and Koivula 1998; Krzemnicki et al., 2001; Schmetzer et al., 2009). Cr^{3+} -bearing pyrope, however, has not been observed in sizes large enough for faceting. In the trade, almost all color-change garnets are referred to as pyrope-spessartine.

A noticeable and attractive color change under

See end of article for About the Authors and Acknowledgments.

GEMS & GEMOLOGY, Vol. 51, No. 4, pp. 348–369,
<http://dx.doi.org/10.5741/GEMS.51.4.348>.

© 2015 Gemological Institute of America



Figure 1. An interesting type of pink pyrope garnet, probably mined in Morogoro, Tanzania, is shown under incandescent light A (left) and daylight-equivalent light D_{65} (right). A noticeable difference in color can be seen. Left to right: a 2.51 ct modified round brilliant faceted by Todd Wacks, a 7.61 ct modified round brilliant faceted by Meg Berry, a 13.09 ct modified round brilliant faceted by Todd Wacks, and 31.90 ct and 6.00 ct rough. The 2.51 ct and 13.09 ct faceted stones were included as part of this study. Photos by Robert Weldon/GIA.

different lighting conditions (i.e., daylight vs. incandescent light) significantly increases the value of a gem, and the decision of whether to apply the “color-change” descriptor is becoming a more important consideration in the trade. The two major systems established to quantitatively analyze color are CIE 1931 (developed in 1931 by the Commission Internationale de l’Éclairage) and CIELAB 1976 (published by the commission in 1976). They have been used to study color-change behavior of pyrope-spessartine garnets from Madagascar (Krzemnicki et al., 2001; Schmetzer et al., 2009). Both articles emphasized that color difference and hue angle difference under various lighting conditions are the most important factors affecting the strength of a stone’s color change (see “Colorimetric Parameters in CIELAB 1976 Color Circle” below).

An interesting observation made after inspecting several faceted stones is that this pink pyrope garnet appears to show a more noticeable “color change” in larger stones. The phenomenon of color-change under a constant lighting but with varying light path length is known as the Usambara effect (Halvorsen and Jensen, 1997; Halvorsen, 2006). Björn (2002) used colorimetric calculations to quantitatively predict the color change caused by the Usambara effect in tourmaline, alexandrite, and color-change garnet. The underlying cause is the relative difference between two transmission windows in the visible absorption spectrum with changing path length.












As noted by previous studies, the presence of two transmission windows in the visible absorption spectrum is also the fundamental cause of a color change under different lighting conditions. Therefore, we

sought to determine how a change in path length influences the color difference and hue angle difference under two lighting conditions and how this relates to the greater difference in color seen in the larger pyropes from this study. Liu et al. (1999b) quantitatively calculated the change of hue angle difference under daylight-equivalent light (D_{65}) and incandescent light (A) in a gem tourmaline with varying thickness from the Uмба Valley, Tanzania. Liu et al. (1999b) suggested that this tourmaline should only be considered a color-change stone within a certain range of path lengths. Schmetzer et al. (2013) studied a synthetic alexandrite crystal and analyzed the relationship between the “alexandrite effect” and the Usambara effect in this pleochroic mineral with varying thickness. To shed more light on this phenomenon, we have carried out a detailed quantitative study of the influence of path length on color difference and hue angle difference under both lighting conditions for three different garnets. In doing so, we developed a new method to correct the UV-Vis-NIR spectra for reflection loss so that spectra for stones with a short path length could be accurately extrapolated to longer path lengths.

MATERIALS AND METHODS

Samples. Twenty-three stones with inclusions provided by Todd Wacks, Jason Doubrava, Jeff Hapeman, and Meg Berry, some of which are shown in figure 1, were used to identify typical inclusions in this material. Among the samples were 21 rough pieces, ranging from 4.04 to 31.90 ct, and two faceted stones weighing 13.88 ct and 13.09 ct. Additionally,

TABLE 1. Chemical composition of pyrope and pyrope-spessartine samples by LA-ICP-MS.

	Pyrope 3	Pk1	Pyrope 11	Pyrope 6	Pyrope 8	Pyrope 9	Pyrope 5	Pyrope 7	Pyrope 10	Bl1	Gr1
											
Carat weight	12.26	2.63	2.51	0.29	0.36	0.67	1.41	1.02	14.79	0.70	0.86
ppmw of different elements											
Mg	125,000	124,000	121,000	117,000	118,000	117,000	120,000	120,000	123,000	83,800	62,100
Ca	16,700	18,400	18,400	15,800	15,100	15,500	19,200	18,100	15,000	14,300	26,100
Mn	45,400	45,800	43,200	57,700	57,700	57,800	42,000	36,700	51,300	134,000	163,000
Fe	32,500	34,300	33,800	31,600	32,400	31,800	35,600	41,200	31,400	18,600	15,600
Al	128,000	132,000	134,000	133,000	133,000	132,000	132,000	136,000	133,000	124,000	119,000
Cr	845	897	697	450	468	476	850	877	615	2210	708
V	1430	1490	1350	947	979	981	1430	1220	1010	5740	5830
Si	197,000	191,000	192,000	191,000	191,000	192,000	194,000	191,000	192,000	183,000	181,000
Ti	358	386	360	299	274	283	362	280	206	453	715
wt.% oxides, converted from LA-ICP-MS											
MgO	20.73	20.56	20.07	19.40	19.57	19.40	19.90	19.90	20.40	13.90	10.30
CaO	2.34	2.57	2.57	2.21	2.11	2.17	2.69	2.53	2.10	2.00	3.65
MnO	5.86	5.91	5.58	7.45	7.45	7.46	5.42	4.74	6.62	17.30	21.05
FeO	4.18	4.41	4.35	4.07	4.17	4.09	4.58	5.30	4.04	2.39	2.01
Al ₂ O ₃	24.19	24.94	25.32	25.13	25.13	24.94	24.94	25.70	25.13	23.43	22.48
Cr ₂ O ₃	0.12	0.13	0.10	0.07	0.07	0.07	0.12	0.13	0.90	0.32	0.10
V ₂ O ₃	0.21	0.22	0.20	0.14	0.14	0.14	0.21	0.18	0.15	0.84	0.86
SiO ₂	42.14	40.86	41.08	40.86	40.86	41.08	41.50	40.86	41.08	39.15	38.72
TiO ₂	0.06	0.06	0.06	0.05	0.05	0.05	0.06	0.05	0.03	0.08	0.12
Total	99.83	99.68	99.32	99.37	99.55	99.40	99.43	99.38	100.45	99.41	99.29
mol.% end members											
Pyrope	72.90	72.64	70.94	68.95	69.43	68.92	70.66	70.42	72.12	51.54	38.90
Grossular	4.69	5.22	5.43	4.84	4.59	4.72	5.61	5.32	4.48	1.12	6.08
Spessartine	11.76	11.86	11.23	15.08	15.07	15.08	10.92	9.55	13.30	36.38	45.26
Almandine	8.28	5.66	8.65	7.93	7.57	7.97	9.09	10.14	6.56	4.02	4.01
Uvarovite	0.35	0.37	0.29	0.19	0.20	0.20	0.35	0.37	0.26	0.96	0.31
Goldmanite	0.73	0.76	0.69	0.49	0.50	0.50	0.73	0.63	0.51	3.07	3.18
Schorlomite-Al	0.16	0.17	0.16	0.13	0.12	0.13	0.16	0.13	0.09	0.21	0.34
Remainder ^a	1.15	3.33	2.63	2.42	2.53	2.50	2.50	3.47	2.68	2.73	1.94
Total	100.00	100.00	100.01	100.01	100.00	100.00	100.01	100.01	100.00	100.01	100.00

^a The “remainder” in the end-member components is what is left over after assigning all the atoms to a stoichiometric garnet formula. This value is related to analytical error in the chemical measurements.

eight rough pyrope specimens, ranging from 0.29 to 14.79 ct, and one 2.51 ct faceted pyrope modified round brilliant were provided by Mr. Wacks for chemical analysis. One blue (Bl1) and one green (Gr1) faceted pyrope-spessartine garnet were selected from the authors’ own collection (table 1) for colorimetric analysis, along with one of the rough pink pyrope samples used for chemical analysis (Pk1). A total of 11 stones underwent chemical analysis as

part of this study. According to Mr. Wacks, this material may have been mined some 30 years ago in Morogoro, Tanzania (Pay, 2015), and could represent the material documented by Stockton (1988).

Standard Gemological Properties. This study began when GIA’s Carlsbad laboratory received a 2.51 ct transparent purple pink modified round brilliant stone for scientific examination (pyrope 11 in table



Figure 2. Three flat wafers with two parallel polished surfaces were prepared and attached in wax to collect UV-Vis-NIR spectra. Wafer Bl1 (left, 1.478 mm in thickness) showed the most intersecting rutile needles in the optical path. Gr1 (middle, 1.416 mm in thickness) showed the fewest interfering rutile needles. The density of the rutile needles blocking the aperture in Pk1 (right, 3.500 mm in thickness) was intermediate between Bl1 and Gr1. Three laser ablation marks are shown in the center of the wafers through the aperture. Photos by Nathan Renfro; fields of view: 11.58 mm (left), 12.17 mm (center), and 14.58 mm (right).

1). Standard gemological testing revealed a refractive index (RI) of 1.736 and no birefringence. The specific gravity (SG), obtained hydrostatically, was 3.75. No fluorescence was observed under either long-wave (LW) or short-wave (SW) UV light. Using a handheld spectroscope, weak absorption lines were observed in the blue and violet section—a 505 nm absorption

In Brief

- Vanadium, chromium, and manganese are responsible for the presence of two visible-light transmission windows in a particular type of pink pyrope garnet. This is the cause of the color difference seen under daylight-equivalent light (D65) and incandescent light (A).
- This material has lower concentrations of vanadium, chromium, and manganese than normal color-change pyrope-spessartine, and a much higher pyrope component. These cause the unique color properties.
- There should be a range of path lengths (sizes) with which the garnet shows the best color change. Below or above this range, the saturation is too low or the hue angle change or saturation change is too small to produce an observable color change.
- There is no unique and simple solution to the problem of classifying color-change stones based on their CIELAB color coordinates, as the entire concept of “color change” is inherently subjective.

line, and very weak absorption bands at 520 and 573 nm. Microscopic examination showed intersecting long and short needles throughout. All of these properties were consistent with pyrope garnet based on the gemological classification system devised by Stockton and Manson (1985). The stone exhibited a noticeable difference in color between incandescent light and daylight-equivalent light.

Photomicrography. The rough stones were fabricated to wafers with parallel windows using standard lapidary equipment, which oriented the inclusions in the best possible position for photomicrography. Photomicrographs were taken using various Nikon microscopes, including an Eclipse LV100, SMZ1500, and SMZ10 (Renfro, 2015a).

Raman Spectroscopy Analysis. Raman spectra were collected with a Renishaw inVia Raman microscope system. The Raman spectra of the inclusions were excited by a Stellar-REN Modu Ar-ion laser producing highly polarized light at 514 nm and collected at a nominal resolution of 3 cm^{-1} in the $2000\text{--}200\text{ cm}^{-1}$ range. Each spectrum of the inclusions was accumulated three times at $20\times$ or $50\times$ magnification. In many cases the confocal capabilities of the Raman system allowed inclusions beneath the surface to be analyzed. Several other stones were polished to expose the inclusion to the surface.

LA-ICP-MS Analysis. The chemical composition for each sample, listed in table 1, was obtained with a ThermoFisher X-series II ICP-MS coupled with a New Wave Research UP-213 laser ablation unit with a frequency-quintupled Nd:YAG laser (213 nm wavelength) running at 4 ns pulse width. NIST (National Institute of Standards and Technology) glass standards SRM 610 and 612 and USGS (United States Geological Survey) glass standards BHVO-2G, BIR-1, NKT-1G, and BCR-2 were used for external calibration. Ablation was achieved using a $55\text{ }\mu\text{m}$ diameter laser spot size, a fluence of around 10 J/cm^2 , and a 15 Hz repetition rate. The garnets were initially internally standardized with ^{29}Si using an educated guess based on the EDXRF analyses. The data was converted to wt.% oxides and normalized to 100 wt. %

and then converted back to ppmw. The ppmw concentration of ^{29}Si obtained in this manner was then used for internal standardization to recalculate the chemical compositions. The ppmw values obtained in this final calculation were identical within <1% to those obtained after normalizing to 100 wt.% with the guessed value of ^{29}Si used for internal standardization, demonstrating the validity of this method. We selected six spots on each pyrope sample for general chemical composition. For the three garnet wafers on which we collected UV-Vis spectra (Pk1, Bl1, and Gr1; see table 1 and figures 2 and 13), the LA-ICP-MS analyses were performed in the same region where the spectroscopic data was collected. The EDXRF data agreed with the LA-ICP-MS analyses, generally within 5–10%.

Energy-Dispersive X-Ray Fluorescence (EDXRF) Analysis. In addition to LA-ICP-MS, the composition of three garnet wafers (Bl1, Gr1, and Pk1) was analyzed on an ARL Quant'X EDXRF analyzer from Thermo Electron Corporation. USGS glass NKT-1G was used for external calibration.

UV-Vis-NIR Spectroscopy. Three garnets (samples Bl1, Gr1, and Pk1) were prepared as wafers with parallel polished surfaces and various thicknesses (figure 2). UV-Vis-NIR spectra were collected with a Hitachi U-2910 spectrometer. The spectra were collected in the 190–1100 nm range with a 1 nm spectral resolution at a scan speed of 400 nm/min.

RESULTS AND DISCUSSION

Microscopic Internal Characteristics. The pink pyrope garnets studied here contain a wide range of inclusions in addition to their interesting color properties. An example is the 13.88 ct faceted pyrope in figure 3, which exhibits a black inclusion that can be seen through the table.

Quartz, apatite, sulfides, graphite, rutile, fingerprint-like inclusions, growth tubes, and negative crystals were observed. Surface features—etch markings and trigons—were also visible. Each type of mineral inclusion was identified by Raman spectroscopy.

Quartz. Quartz is a common inclusion in the pink pyrope garnets from this study. Pyrope-rich garnet is in general associated with magnesium-bearing basic rocks from the lower crust to the upper mantle. In figure 4A, the morphology of a small colorless transparent quartz crystal with conspicuous surface markings appears to be constrained by step-like growth of



Figure 3. A black inclusion with a whitish tension halo rim, likely graphite, was observed under the table facet of the 13.88 ct modified cushion brilliant. The presence of the inclusion makes the stone a collector's piece. The cut stone, faceted by Meg Berry, is shown along with a 43.30 ct rough nodule provided by Jason Doubrava. Photo by Robert Weldon.

the garnet's (110) faces. This crystal is also surrounded by very fine rutile needles, rendering a pseudo-hexagonal contour. This syngenetic crystal showed strong birefringent color under polarized lighting (figure 4B). In figure 4C, some yellowish foreign mineral (possibly goethite, dolomite, or a limonitic mineral) and a tiny black prism (possibly hematite, ilmenite, or senaite) were captured by a transparent quartz crystal. Under polarized lighting, the mineral-filled area showed strong birefringent color (figure 4D). No Raman signal could be obtained for this material, but large clusters of quartz crystal with similar yellowish foreign mineral filler were observed in another stone (figure 4E and 4F). In figure 4G, a very large quartz crystal shows a hexagonal crystal habit. Large quartz crystals with irregular shape were also found (figure 4H). Quartz is also a prevalent mineral inclusion in other garnets such as almandine, umbalite (mainly composed of pyrope and spessartine with small amounts of almandine, lacking color change), and color-change pyrope-spessartine garnet (Gübelin and Koivula, 2005).

Apatite and Other Phosphate Minerals. Apatite and other phosphate minerals have been found in rhodolite, almandine, spessartine, umbalite, and color-change pyrope-spessartine (Gübelin and Koivula, 2005). To isolate the weak apatite Raman scattering signal from the pink garnet host studied here, a bluish

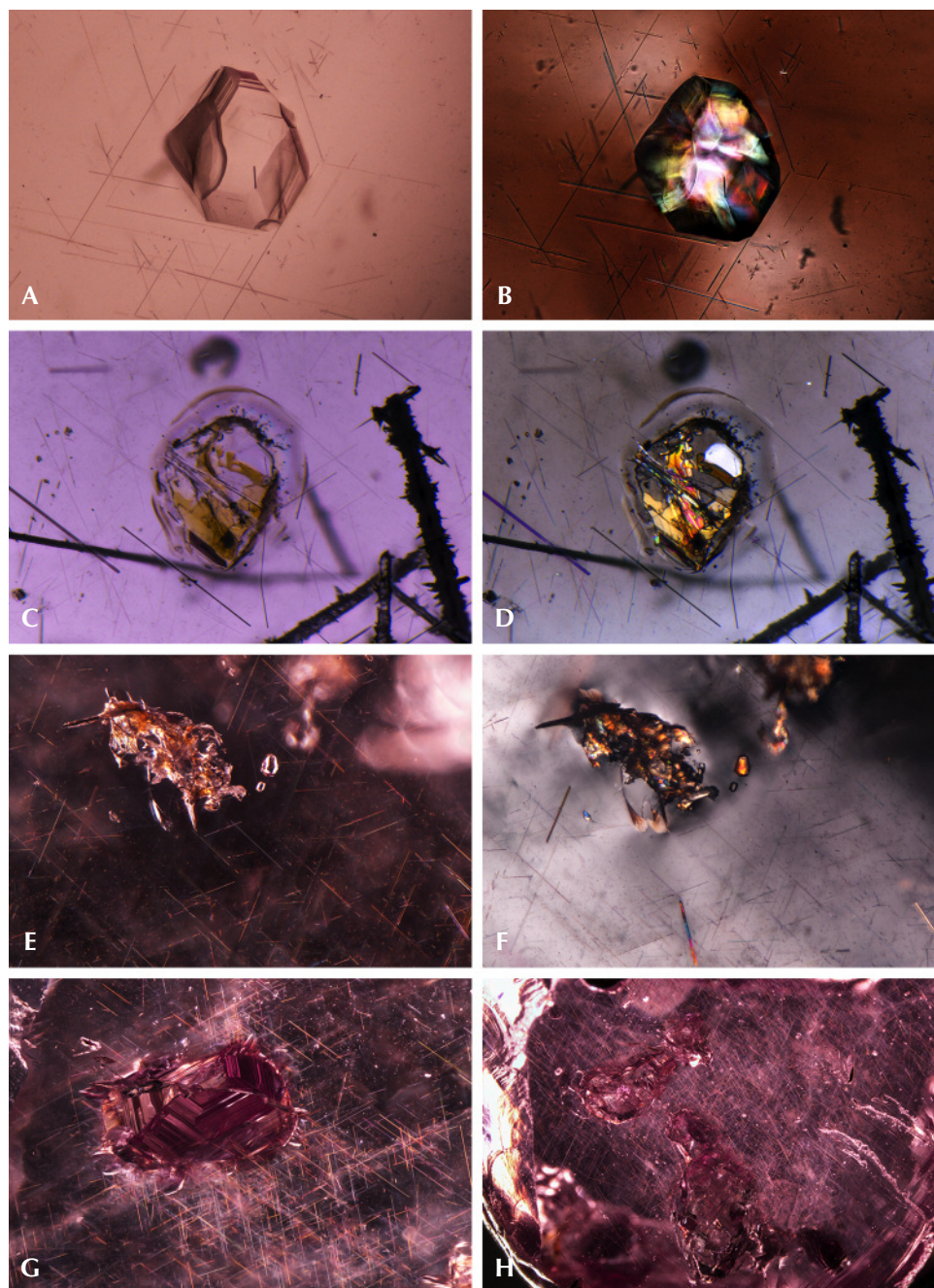


Figure 4. A: Transparent quartz crystal with sharp euhedral crystal faces under diffused transmitted lighting. B: The same crystal with bright interference colors under cross-polarized lighting. C: Quartz crystal filled with foreign yellowish material under diffused transmitted lighting. D: The foreign yellowish material showed interference colors under cross-polarized lighting. E: Cluster of quartz crystals with foreign yellowish material under darkfield illumination. F: The quartz host and foreign yellowish material both showed interference colors under cross-polarized light. G: The hexagonal geometry of a large quartz crystal became very distinct under darkfield illumination. H: Two large quartz crystals with irregular shape under darkfield illumination. Fields of view: 0.62 mm (A and B), 1.92 mm (C and D), 1.99 mm (E and F), 2.34 mm (G), and 7.19 mm (H). Photomicrographs Ziyin Sun (A and B), Nathan Renfro (C and D), and Jonathan Muyal (E–H).

hexagonal prismatic apatite crystal was partially polished through to reach the surface (figure 5A). The outline of the crystal was distinct under polarized lighting (figure 5B). Figures 5C and 5D show a group of rounded apatite crystals whose morphology suggests they were partially corroded before being captured by the garnet. An extremely large euhedral apatite crystal showed a greenish yellow bodycolor (figure 5E) with a fingerprint-like halo extending around its perimeter. Another whitish mineral gave

an unidentifiable Raman spectrum, which nonetheless seemed to share many similarities with Raman spectra of other phosphate minerals (figure 5F).

Sulfides. Sulfide crystals are another very common mineral inclusion in these pink pyrope garnets. Raman spectroscopy was inconclusive, even when the inclusions were polished to the surface; the closest match was for chalcocite, although other sulfides and sulfosalts gave reasonable matches as well. Figure

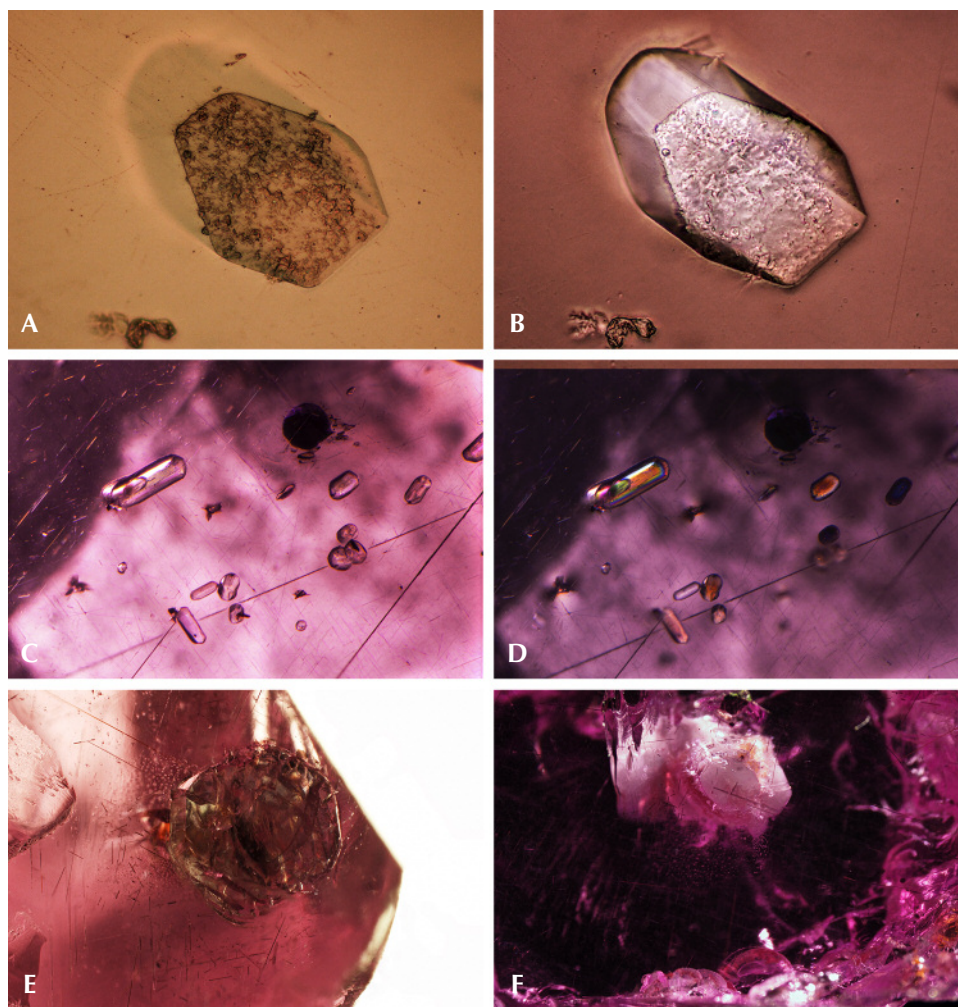


Figure 5. A: This bluish apatite crystal, shown in reflected lighting and weak diffused transmitted lighting, displays a hexagonal crystal outline where it breaks the surface. B: The entire shape of the same crystal is distinct under cross-polarized lighting. C: This group of rounded apatite crystals is shown under diffused transmitted lighting. D: All the crystals in 5C showed interference colors under cross-polarized lighting. E: This large greenish yellow tabular apatite crystal with a liquid fingerprint extending from it is seen in diffused transmitted and fiber-optic lighting. F: A large opaque whitish phosphate mineral under darkfield illumination. Fields of view: 0.25 mm (A and B), 2.52 mm (C and D), 4.92 mm (E), and 7.19 mm (F). Photomicrographs Ziyin Sun (A, B, and E), Nathan Renfro (C and D), and Jonathan Muyal (F).

6A shows a rounded sulfide crystal that was partially exposed and showed a metallic luster under reflected light. The depression next to the crystal suggests that there was originally another sulfide crystal. The crystal outline is distinct under darkfield illumination (figure 6B). All the sulfides showed a reddish reflected color when illuminated by a fiber-optic light from the side of the wafer (figure 6C, 6D, and 6E), although this may represent the red color of the light transmitted through the garnet. Some of these inclusions have associated fingerprint-like inclusions showing birefringent color under cross-polarized lighting (figure 6F and 6G), and many are surrounded by clusters of rutile needles (figure 6F). An orange iron oxide mineral is also associated with fractures near some of these sulfide inclusions (figure 6F). The flow lines next to the rutile cluster on the top part of figure 6G may be the result of excess titanium in the mineralization environment, which causes TiO_2 to precipitate and coalesce as “silk” as the garnet cools.

Graphite. Black tablets of graphite represent one of the more frequent inclusions of the pink pyrope garnets in this study. The partially exposed graphite crystal in figure 7A showed a dull luster. The outline of the crystal and a surrounding tension halo became distinct under darkfield illumination (figure 7B). Some of the graphite showed a very uniform layered pseudohexagonal crystal structure (figure 7C). The whitish tension halo is always present around the graphite (figure 7C). The presence of graphite suggests a relatively high-grade metamorphic formation process. It is also a frequent guest mineral in almandine and color-change pyrope-spessartine. The common association of V-bearing gem material with graphite, as found in this pink pyrope in many gem-bearing metamorphic deposits from East Africa (e.g., tanzanite and tsavorite), is of interest.

Rutile. Strong fiber-optic lighting revealed a three-dimensional network of (presumably) rutile needles and unknown mineral platelets that showed flashes of iri-

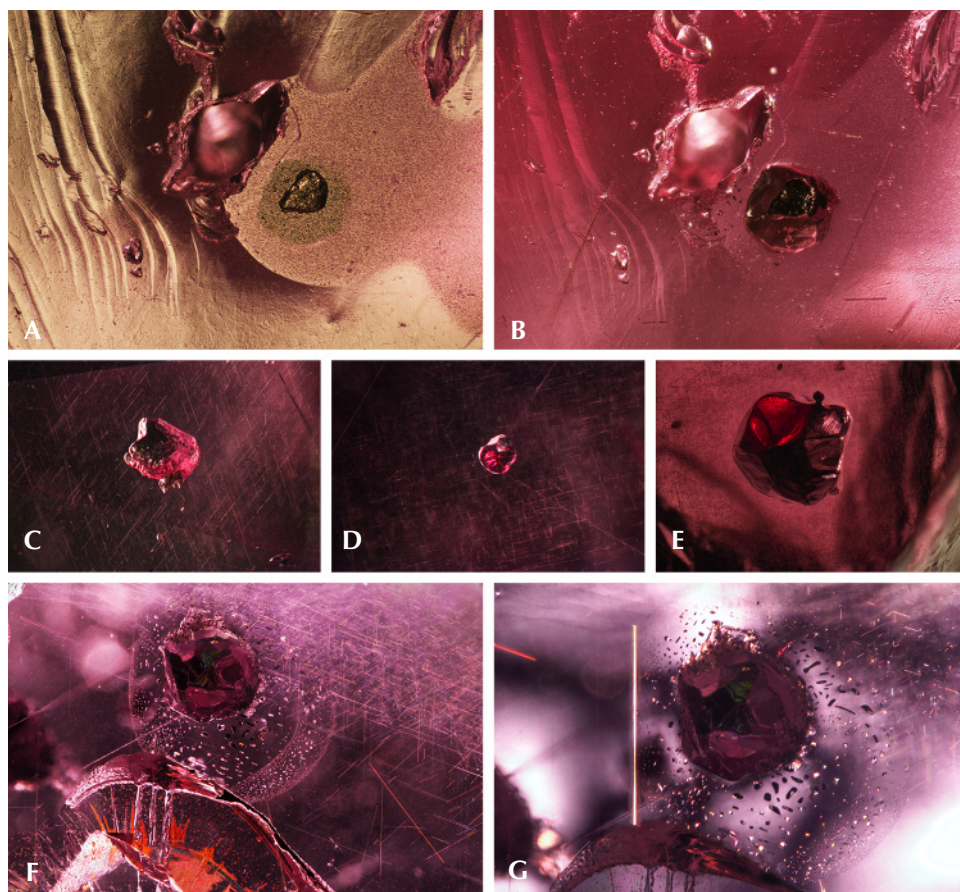


Figure 6. A: An opening next to a surface-reaching sulfide crystal, shown under reflected lighting and weak transmitted lighting. B: The outline of the crystal became distinct under darkfield illumination. C, D, and E: These sulfides showed reddish color when illuminated with strong fiber-optic lighting from the side. F: This well-formed sulfide crystal with extended partially healed tension halo is shown under darkfield and fiber-optic illumination. G: Fingerprint-like inclusions in the partially healed tension halo displayed birefringent color under cross-polarized lighting. Fields of view: 2.47 mm (A and B), 2.96 mm (C and D), 5.85 mm (E), 3.57 mm (F), and 2.85 mm (G). Photomicrographs by Ziyin Sun (A, B, and E), Aaron C. Palke, (C and D), and Jonathan Muiyal (F and G).

descent color (figure 8A). The slender needles appeared to outline the edges of a rhombododecahedron (probably aligned along $\langle 110 \rangle$). Under cross-polarized lighting, the needles showed birefringent color (figure 8B). One blocky rutile crystal that presented itself along a fracture surface appeared to have a metallic luster under reflected lighting (figure 8C). Observing

this mineral from the opposite side revealed how it would look like as an inclusion in a stone (figure 8D). This blocky rutile crystal appeared black and opaque.

Fingerprint-Like Inclusions. Fingerprint-like fluid inclusions are common features in the pyrope garnets. In figure 9A, a large secondary inclusion plane is

Figure 7. A: This graphite crystal with tension halo is shown under reflected lighting and weak diffused transmitted lighting. B: The outline of the same black graphite crystal became distinct under darkfield illumination. C: The layered structure of the graphite inclusion is visible under diffused fiber-optic lighting. Fields of view: 1.24 mm (A and B) and 0.62 mm (C). Photomicrographs by Jonathan Muiyal and Ziyin Sun.



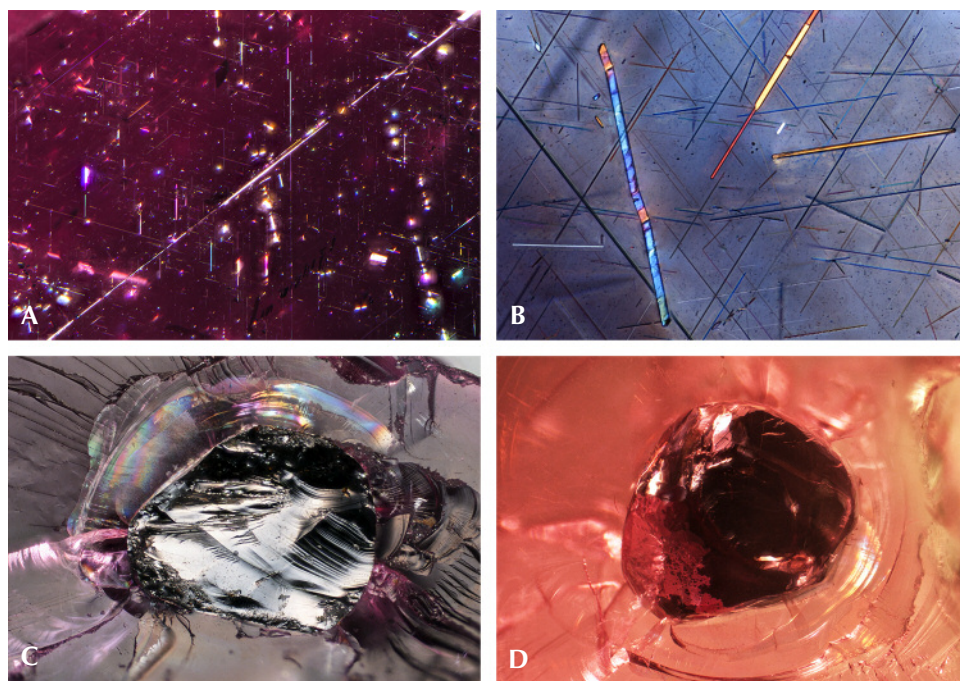


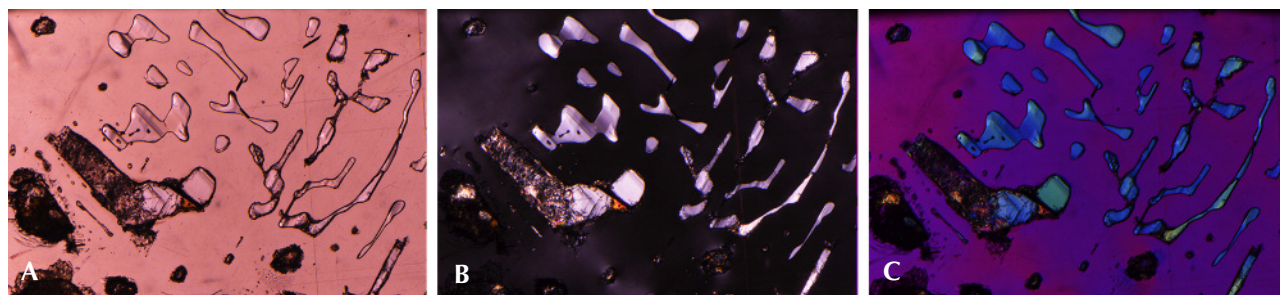
Figure 8. A: Iridescent intersecting rutile needles under fiber-optic illumination. B: Three needle-like mineral inclusions showing birefringent color under cross-polarized lighting. C: A large rutile crystal breaking the surface shows a metallic luster under reflected lighting. D: The same crystal observed from the opposite side under darkfield illumination. Fields of view: 3.48 mm (A), 0.62 mm (B), and 2.47 mm (C and D). Photomicrographs by Nathan Renfro (A), Jonathan Muiyal (B), and Ziyin Sun (C and D).

partly filled by some foreign material, possibly quartz. Viewed in cross-polarized light, the inclusions appear to show birefringent colors, suggesting the presence of some mineral phase that presumably precipitated from the fluid that originally occupied a partially healed fracture plane (figure 9B). The interference colors in this photomicrograph are all of low intensity, and the image is quite dark. The picture immediately takes on an array of vivid colors with the insertion of the first-order red compensator (figure 9C; see Koivula, 1984; Renfro, 2015a).

Growth Tubes and Negative Crystals. These pink pyrope garnets are also characterized by the presence of

many hollow tubes whose sides appear to be confined by the crystal structure. It is possible that rutile or another needle-like mineral inclusion originally occupied these spaces but was later dissolved. Alternatively, these could be growth tubes caused by some defect in the crystal lattice that blocked garnet growth in a specific zone while the bulk of the garnet continued to grow around it, resulting in a hollow tube. Many of the hollow tubes were later filled with epigenetic yellowish limonitic material (figure 10, left). Some tabular rounded negative crystals were also observed (figure 10, right). Those voids do not show an interference color under cross-polarized lighting and are thus probably filled with some fluid or vapor phase.

Figure 9. A: Partially healed fingerprint-like inclusions under diffused transmitted lighting. B: The same inclusion under polarized lighting. C: The same inclusion under polarized lighting with insertion of the first-order red compensator. Field of view: 3.16 mm. Photomicrographs by Nathan Renfro.



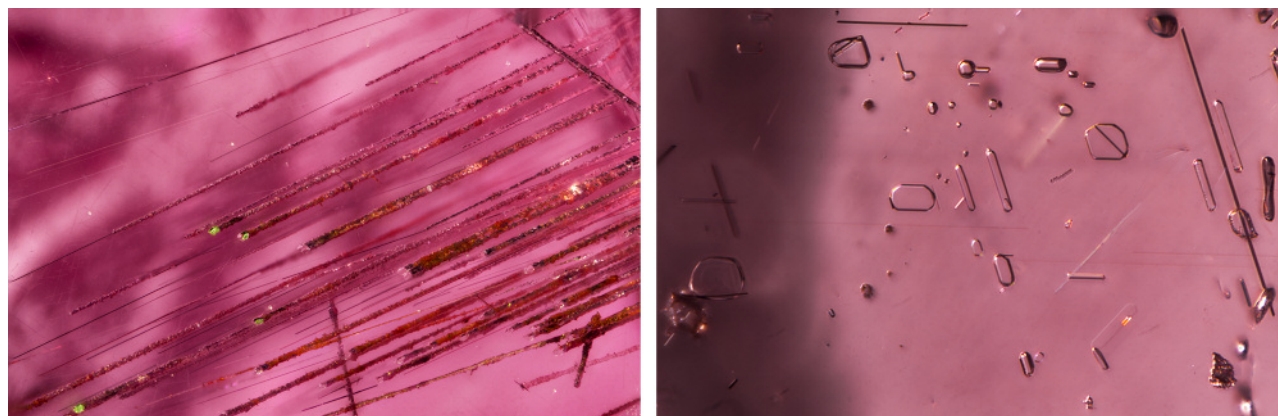
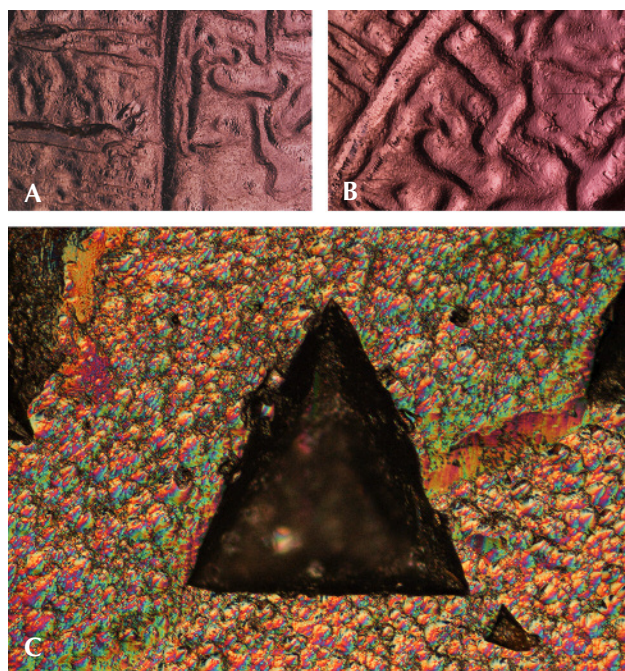


Figure 10. Left: Hollow growth tubes filled with limonitic iron compound minerals, viewed in diffused transmitted and fiber-optic illumination. Right: Rounded negative crystals and voids viewed in diffused transmitted illumination. Fields of view: 4.33 mm (left) and 1.26 mm (right). Photomicrographs by Nathan Renfro (left) and Jonathan Moyal (right).

Surface Features: Etch Markings and Trignons. Unusual slightly rounded and circuitous channels were observed on the surface of one piece of pink garnet rough. To our knowledge, such a pattern has not been

Figure 11. A: Numerous channels on the surface of a garnet rough under diffused reflected lighting. B: The same channels, seen at higher magnification under diffused reflected lighting. C: An episcopic differential interference contrast (DIC) image of large trigons on the surface of a garnet rough under reflected lighting. Fields of view: 5.98 mm (a), 4.79 mm (b), and 0.62 mm (c). Photomicrographs by Nathan Renfro.



described in garnet or any other gem material. One possible explanation is that a larger piece of garnet broke along a large secondary fluid inclusion plane, and the pattern left by the fluid inclusion plane was corroded and rounded, ultimately forming the channels seen in figures 11A and 11B. Other fresh pink pyrope surfaces show trigon-shaped depressions that can be effectively imaged using episcopic differential interference contrast (DIC), as shown in figure 11C (see also Koivula, 2000; Renfro, 2015b). The formation process of those large trigons is still unknown, although such features are presumed to be caused by late-stage dissolution or etching.

The inclusions observed suggest that this pink pyrope garnet is a product of high-grade metamorphic formation processes. Weak to strong corrosion probably also occurred sometime after the crystal growth, likely after peak metamorphic conditions.

Chemical Analysis. Table 1 shows the chemical composition of nine pyrope and two pyrope-spessartine garnets, expressed as ppmw (parts per million by weight), oxide percent by weight (as derived from ppmw values from LA-ICP-MS measurements; other trace elements are not reported here), and mole percent end members (mol.%), calculated using the spreadsheet method of Locock (2008). We conclude that this type of pink pyrope garnet has the following end-member composition: pyrope 68.92–72.90 mol.%, grossular 4.48–5.61 mol.%, spessartine 9.55–15.08 mol.%, almandine 5.66–10.14 mol.%, uvarovite 0.19–0.37 mol.%, and goldmanite 0.49–0.76 mol.%. The composition of two pyrope-spessartine garnets (Bl1 and Gr1) is also listed for comparison in table 1. As a secondary check on the

accuracy of the LA-ICP-MS results, the composition of the three garnet wafers (Bl1, Gr1, and Pk1) was also analyzed by EDXRF. The EDXRF results generally agreed with the LA-ICP-MS measurements within 5–10% for the elements listed in table 1.

Visible Absorption Spectrum Analysis. Accurate visible spectroscopic measurement relies on correctly identifying the spectral baseline. This is especially true in the present study, where spectra for stones with long path lengths were produced by multiplying the spectrum collected from thin wafers (approximately 1–4 mm) by an appropriate factor. In this case, the baseline must be carefully corrected to avoid amplifying any errors inherent in fitting the baseline.

Absorbance, A , in our UV-Vis-NIR spectra is the sum of A_c (chromophore light loss), A_{rl} (reflection light loss, surface of the gem), and A_{isl} (inclusion-scattering light loss). An equation can be written simply as

$$A = A_c + A_{rl} + A_{isl} \quad (1)$$

Samples Bl1, Gr1, and Pk1 were polished into wafers with thicknesses of 1.478, 1.416, and 3.500 mm, respectively. After UV-Vis-NIR spectra were collected (red traces in figure 12), the three wafers were further polished down to thicknesses of 0.906, 0.842, and 2.278 mm. UV-Vis-NIR spectra were collected on the thinner wafers (green traces in figure 12). When the short path length traces are subtracted from the long path length traces, the resulting spectra (blue traces in figure 12) have the A_{rl} reflection light loss removed because A_{rl} is expected to be the same regardless of the stone's thickness. These spectra, corrected for reflection light loss, correspond to path lengths equal to the difference between the long and short path lengths for each stone. Now we can use these reflection-corrected spectra to produce the spectra of any desired path length by multiplying by an appropriate constant. We can also calculate the spectra of the reflection light loss (purple traces in figure 12) by renormalizing the reflection-corrected spectra to the original path lengths and taking the difference between the corrected and uncorrected spectra, as discussed below.

The baselines of the reflection-corrected spectra are not equal to 0 at 850 nm, which would be expected with an absolutely perfect correction. The magnitude of the residual baseline correlates with the relative amount of rutile inclusions observed in the garnets, with Bl1 having the highest concentration and Gr1 the

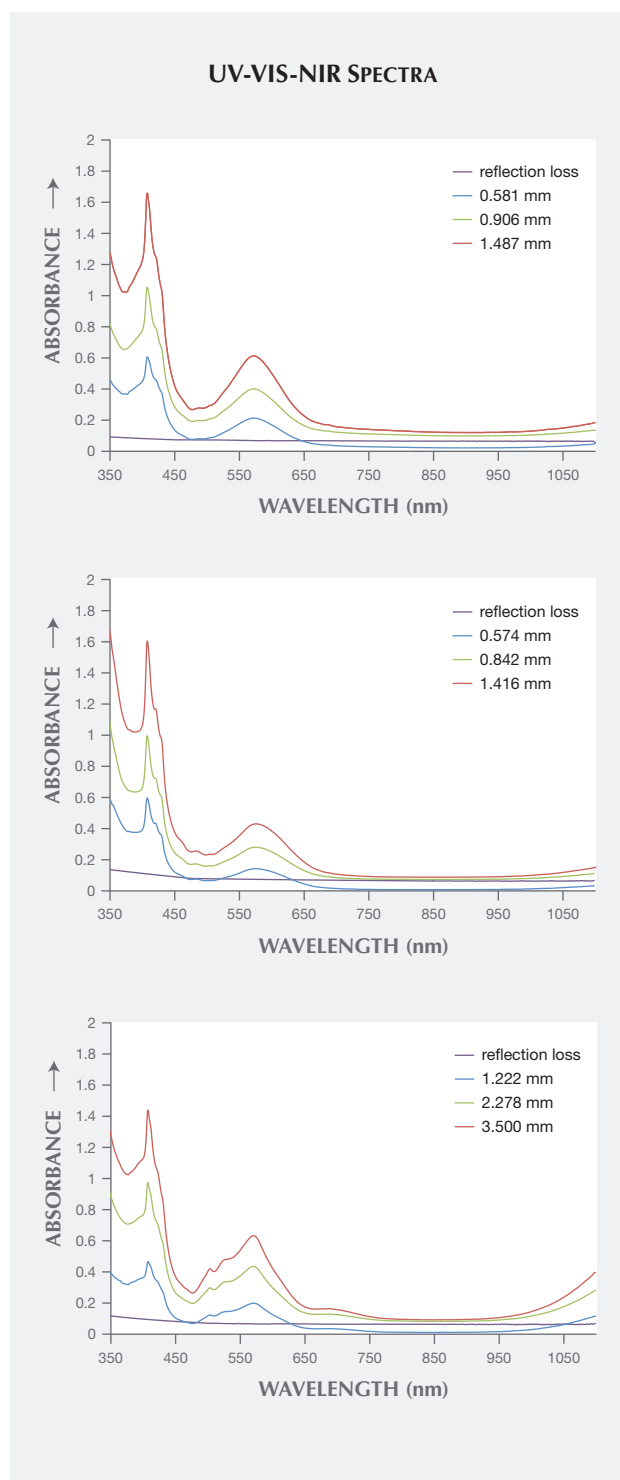


Figure 12. For samples Bl1 (top), Gr1 (middle), and Pk1 (bottom), the red traces are the absorption spectra for the wafer. The green traces are the absorption spectra for the same wafer polished down to a thickness of 0.906, 0.842, and 2.278 mm. The blue traces are the absorption spectra created by subtracting the green traces from the red traces. Finally, the purple traces are the spectra of the reflection light loss.

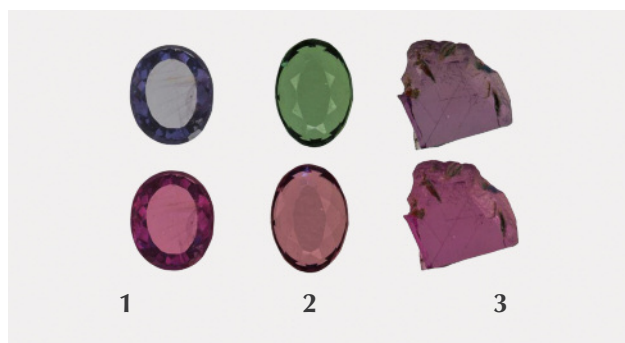


Figure 13. These photos show polished wafers under daylight-equivalent light (top) and incandescent light (bottom). Left to right: Samples Bl1 (1.487 mm thick), Gr1 (1.416 mm thick), and Pk1 (3.500 mm thick). Composite photo by Robison McMurtry.

lowest. Thus, we can conclude that the residual baseline is mainly caused by inclusion-scattering absorption (A_{isl} in equation 1). Note that no attempt is made to correct the spectra for A_{isl} . If we assume that light scattering particles are evenly distributed and have uniform orientation, size, and shape within a certain stone, then the magnitude of this term is expected to be dependent on the thickness of the stone. While this assumption will not be strictly correct for most gem

materials, a more rigorous correction for A_{isl} is not feasible at the moment, and will probably not have a significant impact on the results.

The calculated visible spectra for samples Bl1, Gr1, and Pk1 share many of the same features, as shown in figures 13 and 14. The absorption bands at 410, 422, and 430 nm are caused by Mn^{2+} , while those at 504 and 521 nm are caused by Fe^{2+} (Moore and White, 1972). A wide absorption band between 550 and 600 nm is caused by contributions from both Cr^{3+} and V^{3+} (Geiger et al., 2000). Sample Bl1 shows two transmission windows: Window A lies in the red section from 650 to 700 nm; window C, with its transmission maximum at 477 nm, lies in the blue section of the spectrum (figure 14). Sample Gr1 shows the same transmission window in the red section of the spectrum (window A), but the higher-energy transmission window is more open to wavelengths of light in the green section, with its transmission maximum at 510 nm (window B). The red transmission window for Pk1 is wider than for the other two samples. The higher-energy window has a transmission maximum at 477 nm, similar to Bl1, but with more transmission in the higher-energy (violet) section due to the lower Mn^{2+} content (again,

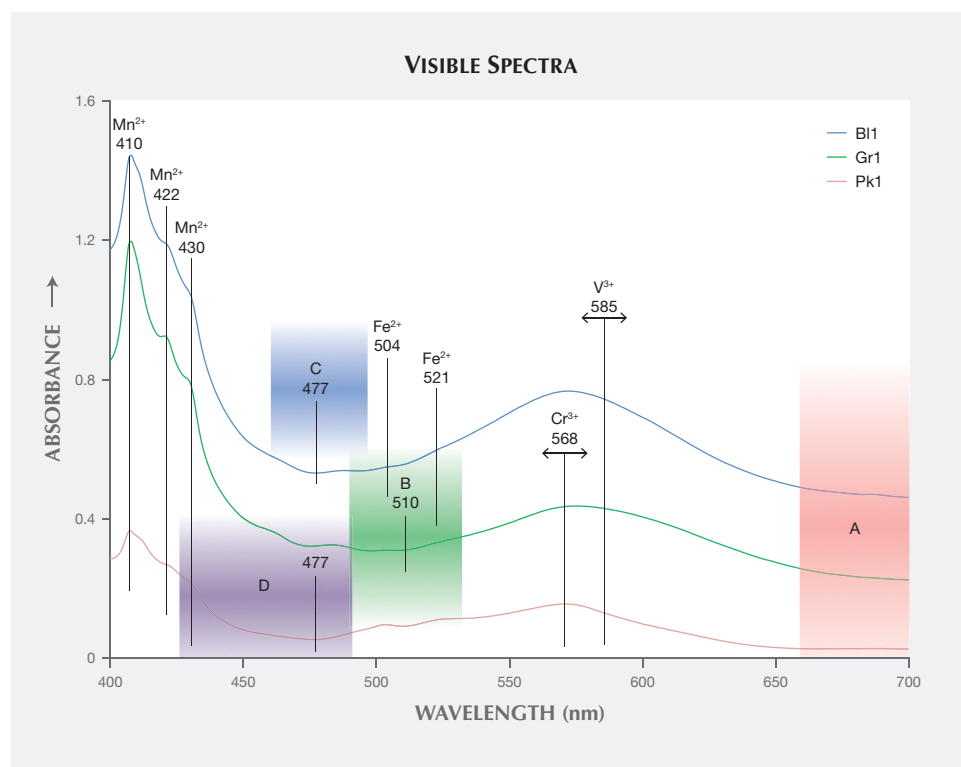


Figure 14. The calculated visible absorption spectra of three garnets with 1 mm thickness revealed absorption bands at 410, 422, and 430 nm caused by Mn^{2+} ; absorption bands at 504 and 521 nm caused by Fe^{2+} ; and a wide absorption band between 550 and 600 nm caused by Cr^{3+} and V^{3+} . Transmission windows A, B, C, and D are labeled. The green trace and the blue trace are offset by 0.2 and 0.4 absorbance units, respectively.

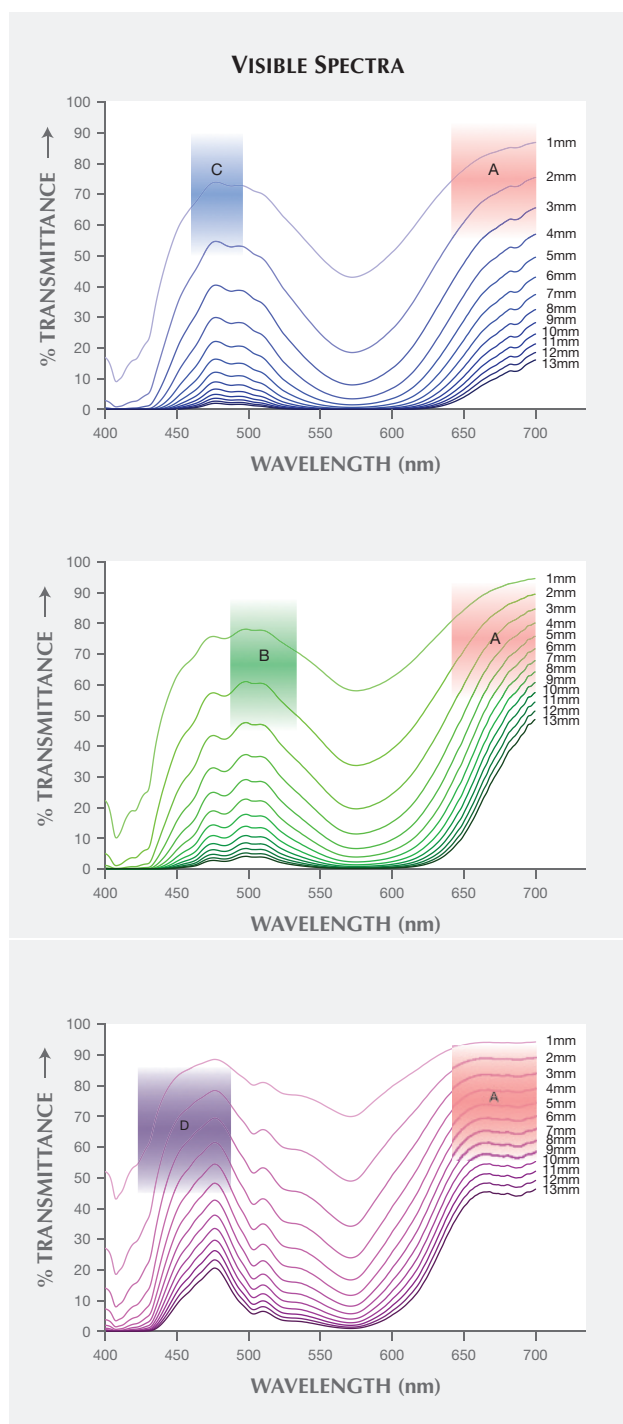


Figure 15. Top: Visible transmission spectra of Bl1 with path length from 1 to 13 mm; transmission windows A and C become smaller with increasing wafer thickness. Middle: Visible transmission spectra of Gr1 with path length from 1 to 13 mm; transmission windows A and B become smaller with increasing wafer thickness. Bottom: Visible transmission spectra of Pk1 with path length from 1 to 13 mm; transmission windows A and D become smaller with increasing wafer thickness.

see figure 14). The transmission windows described here are similar to those mentioned by Schmetzer et al. (2009).

SPECTRUM AND COLORIMETRIC DATA ANALYSIS

Visible Transmission Spectra. The spectra of three garnets were converted to transmission spectra with path lengths from 1 to 13 mm by multiplying the spectra by an appropriate value (l/l_0 , where “ l ” is the desired path length and “ l_0 ” is the path length of the reflection-corrected spectrum—0.581 mm, 0.574 mm, and 1.222 mm for Bl1, Gr1, and Pk1, respectively). For all samples, the transmission windows became smaller as the path length increased (figure 15). CIELAB 1976 L^* , a^* , b^* color space coordinates were calculated for each spectrum under incandescent and daylight-equivalent light with the GRAMS software using the relative spectral power distribution of CIE standard illuminant D_{65} and A, and CIE 1931 2° standard observer (CIE, 2004).

Colorimetric Parameters in CIELAB 1976 Color Circle. Thorough discussions of the principles behind the CIELAB 1976 color circle have appeared elsewhere (CIE, 2004; Schmetzer et al., 2009). Therefore, we present a brief introduction and direct the reader to other sources for more detailed explanations.

The color circle has three axes in a three-dimensional space. L^* represents lightness and is perpendicular to the plane of the paper. A low L^* value signifies a darker color, a high value a lighter color. The variables a^* and b^* lie in the plane of the paper and define a two-dimensional Cartesian coordinate system that represents the different colors and color saturations possible within the color circle. The coordinates a^* and b^* can also be converted to polar coordinates C^*_{ab} and h_{ab} .

The variable C^*_{ab} represents chroma or saturation, and a higher C^*_{ab} value means a more saturated color. It is calculated by the equation

$$C^*_{ab} = \sqrt{a^{*2} + b^{*2}}$$

The hue angle, h_{ab} , is calculated by the equation

$$h_{ab} = \arctan(a^*/b^*)$$

Variations in h_{ab} cause changes in hue, starting from purple-red at 0°, yellow at 90°, bluish green at 180°, and blue at 270°.

Finally, E^*_{ab} signifies the geometric distance of a specific $L^*a^*b^*$ color coordinate in three-dimensional

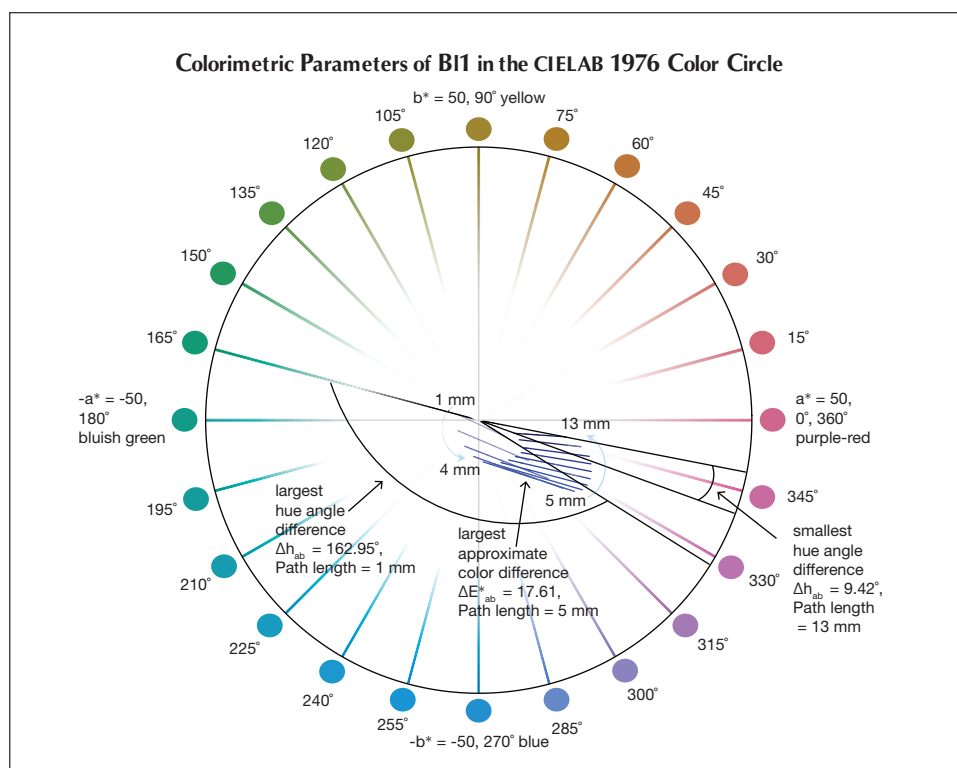


Figure 16. B11 showed the largest approximate color difference $\Delta E^*_{ab} = 17.61$ at a path length of 5 mm, the largest hue angle difference $\Delta h_{ab} = 162.95^\circ$ at a path length of 1 mm, and the smallest hue angle difference $\Delta h_{ab} = 9.42^\circ$ at a path length of 13 mm.

CIELAB color space from the origin at $L^* = 0$, $a^* = 0$, and $b^* = 0$. E^*_{ab} is calculated by the equation

$$E^*_{ab} = \sqrt{a^{*2} + b^{*2} + L^{*2}}$$

The utility of E^*_{ab} lies in the fact that the difference in this value for two different color coordinates, ΔE^*_{ab} , is a reliable measurement of the absolute color difference between, for instance, the color of a stone under two different lighting conditions.

The color difference between daylight-equivalent (D_{65}) and incandescent (A) lighting, ΔE^*_{ab} , is calculated by the equation

$$\Delta E^*_{ab} = \sqrt{\Delta a^{*2} + \Delta b^{*2} + \Delta L^{*2}}$$

where $\Delta a^* = a^*_{D65} - a^*_{A}$, $\Delta b^* = b^*_{D65} - b^*_{A}$, and $\Delta L^* = L^*_{D65} - L^*_{A}$.

$\Delta h_{ab}(\circ)$, the hue angle difference between daylight-equivalent (D_{65}) and incandescent (A) lighting, is calculated by the equation

$$\Delta h_{ab} = |h_{ab,D65} - h_{ab,A}|$$

ΔC^*_{ab} , the chroma (saturation) difference between daylight-equivalent and incandescent lighting, is calculated by the equation

$$\Delta C^*_{ab} = |C^*_{ab,D65} - C^*_{ab,A}|$$

Table 2 shows values of C^*_{ab} , h_{ab} , ΔC^*_{ab} , Δh_{ab} , and ΔE^*_{ab} of three garnet samples (Pk1, B11, and Gr1) under daylight-equivalent and incandescent lighting with path lengths from 1 to 13 mm.

The CIELAB 1976 Color Circle Plots (Schmetzer et al., 2009 and 2013). A convenient way to represent the color difference between daylight-equivalent (D_{65}) and incandescent (A) lighting for a sample is to project the three-dimensional $L^*a^*b^*$ coordinates into the two-dimensional a^*b^* plane (the color circle) and draw a tie-line between the D_{65} and A lighting coordinates. Furthermore, if one wants to track the color difference between D_{65} and A lighting with increasing light path length, such tie lines could be drawn for each path length and plotted on the same color circle. We did so for garnet samples B11, Gr1, and Pk1, with path lengths from 1 to 13 mm (figures 16–18). The right ends of the tie lines represent the color coordinates under incandescent lighting (A). The left ends of the tie lines represent the color coordinates under daylight-equivalent lighting (D_{65}).

Alternatively, one could isolate a specific variable such as ΔE^*_{ab} , Δh_{ab} , or ΔC^*_{ab} and plot its changes with the light path length. Such plots are shown for samples Pk1, B11, and Gr1 in figure 19. All three show similar behavior in their color difference vs. path

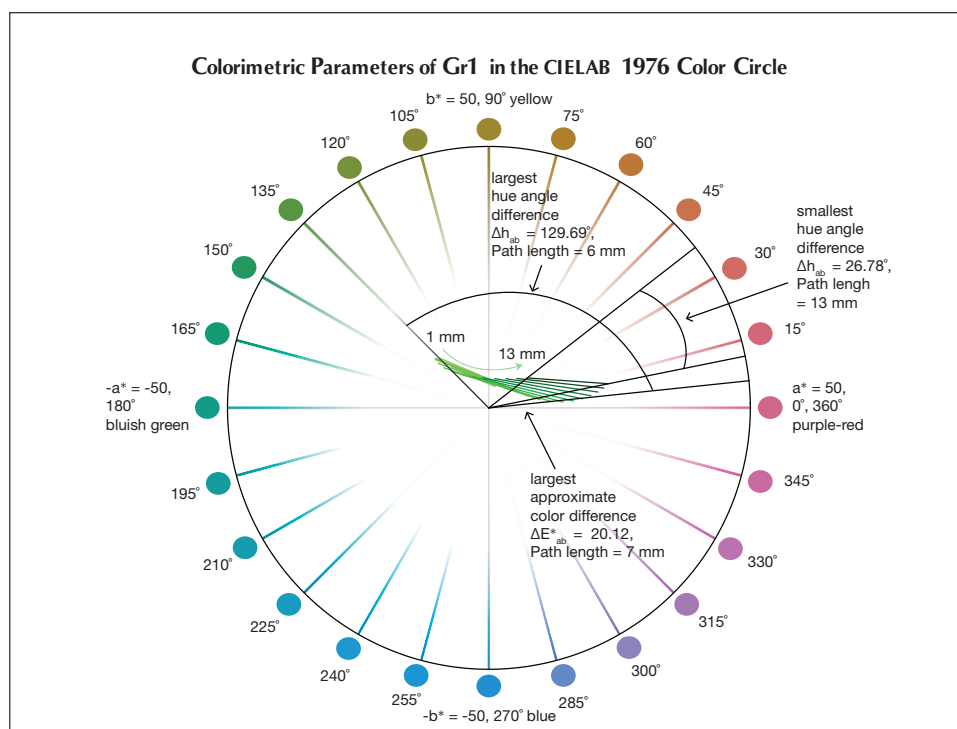


Figure 17. Gr1 showed the largest approximate color difference $E^*_{ab} = 20.12$ at a path length of 7 mm, the largest hue angle difference $\Delta h_{ab} = 129.69^\circ$ at a path length of 6 mm, and the smallest hue angle difference $\Delta h_{ab} = 26.78^\circ$ at a path length of 13 mm.

length plots, with ΔE^*_{ab} steadily rising with path length until reaching a critical point and falling again (figure 19, left column). However, these three stones all showed different behavior in hue angle

vs. path length plots and chroma difference vs. path length plots (figure 19, center and right columns). The hue angle difference Δh_{ab} of sample B11 decreases steadily as the stone becomes thicker. The hue angle

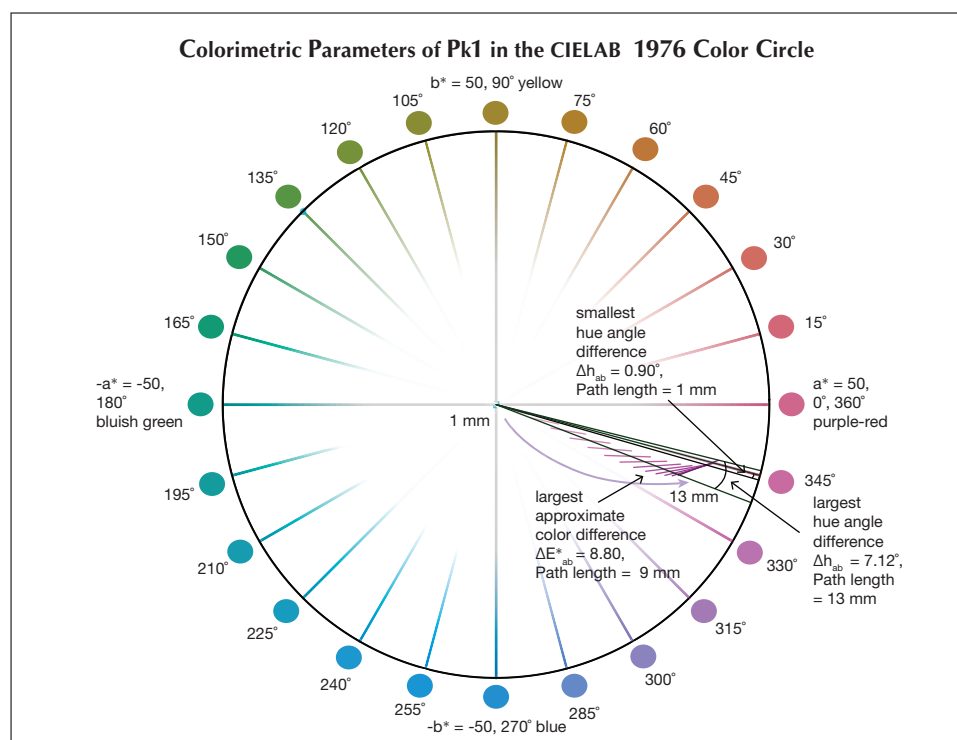


Figure 18. Pk1 showed the largest approximate color difference $\Delta E^*_{ab} = 8.80$ at a path length of 9 mm, the largest hue angle difference $\Delta h_{ab} = 7.12^\circ$ at a path length of 13 mm, and the smallest hue angle difference $\Delta h_{ab} = 0.90^\circ$ at a path length of 1 mm. The path length = 1 mm tie line is obscured because it is almost parallel to the black lines indicating the smallest hue angle.

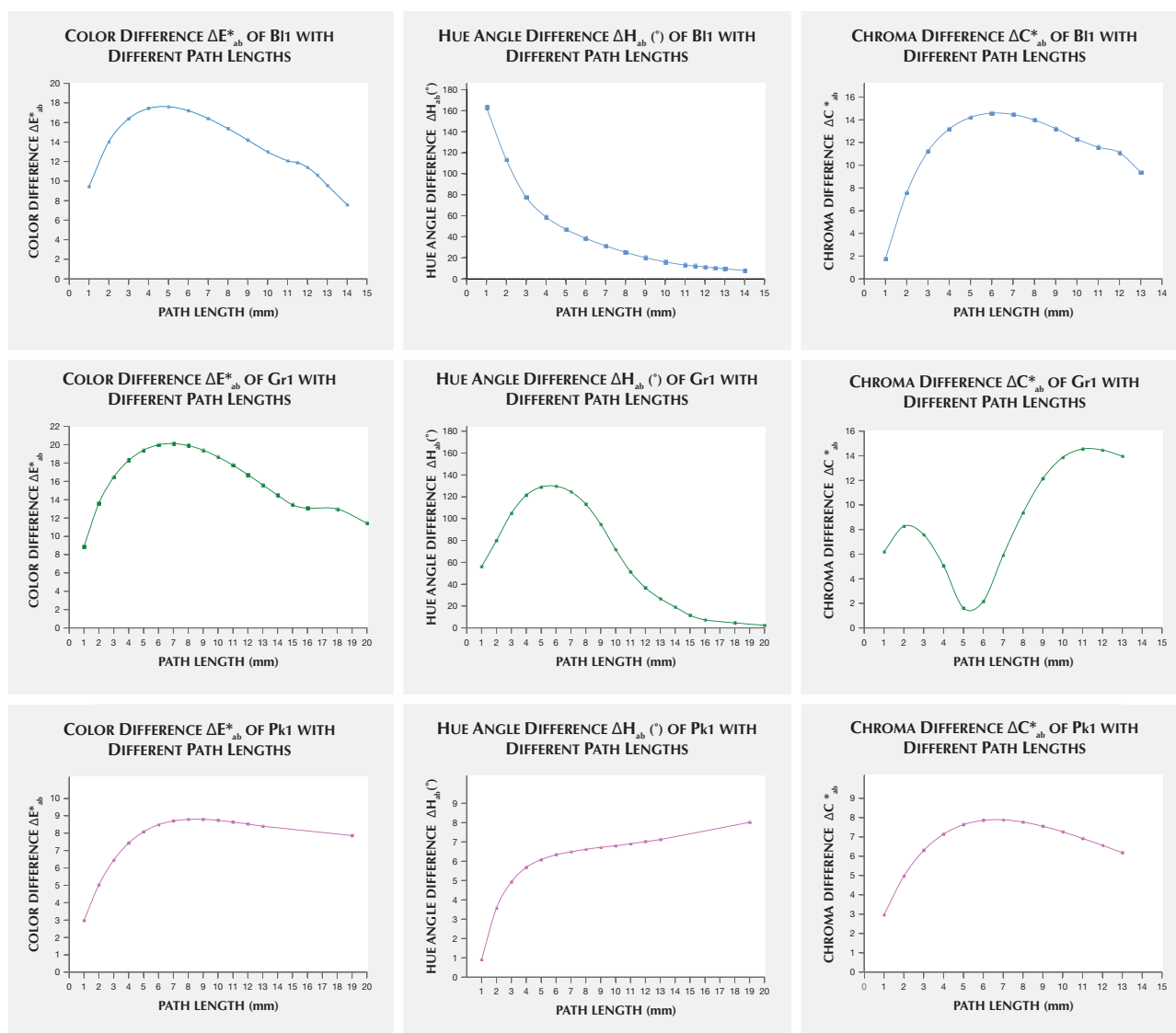


Figure 19. The color difference vs. path length, hue angle difference vs. path length, and chroma difference vs. path length plots of Bt1 (top row) show that ΔE^*_{ab} and ΔC^*_{ab} reach their maximum at a path length of 5 mm and 6 mm, respectively, and ΔH_{ab} continues to decrease as path length increases. For Gr1 (middle row), ΔE^*_{ab} , ΔH_{ab} , and ΔC^*_{ab} reach their maximum at path lengths of 7 mm, 6 mm, and 10 mm, respectively. For Pk1 (bottom row), ΔE^*_{ab} and ΔC^*_{ab} reach their peak at path lengths of 9 mm and 6 mm, respectively, and ΔH_{ab} continues to increase with path length.

difference ΔH_{ab} of Gr1 increases until reaching its highest value when the path length is 6 mm, after which it begins to decrease. On the other hand, the hue angle difference ΔH_{ab} of Pk1 simply continues to rise with the thickness of the stone until reaching a 13 mm path length (figure 19, middle column). The chroma difference ΔC^*_{ab} of Bt1 and Pk1 increases until reaching their maximum values, after which they decrease again (figure 19, right column, top and bottom rows). The chroma difference ΔC^*_{ab} of Gr1 increases first, then decreases before rising again to

form a wave shape (figure 19, right column, middle row). At greater path length, the magnitude of the color change increases at first as the chroma (saturation), chroma difference, or hue angle difference increases and then decreases as the chroma, chroma difference, or hue angle difference decreases. This occurs because one of the transmission windows is preferentially “closed” as the stone becomes thicker. This type of behavior is related to the strength of two transmission windows (figure 14) and the complex relationship between them. It is difficult to predict

TABLE 2. Colorimetric data of three garnets with wafer thickness from 1 to 13 mm.

Path Length		Bl1	Gr1	Pk1	Path Length		Bl1	Gr1	Pk1
1 mm	L* for daylight D ₆₅	79.33	85.59	90.54	6 mm	L* for daylight D ₆₅	26.13	39.59	55.61
	a* for daylight D ₆₅	-3.76	-6.97	3.07		a* for daylight D ₆₅	2.54	-7.07	19.88
	b* for daylight D ₆₅	0.99	7.89	-0.90		b* for daylight D ₆₅	-7.97	6.99	-9.28
	L* for incandescent light A	78.94	85.32	90.77		L* for incandescent light A	25.92	39.34	57.09
	a* for incandescent light A	4.79	1.10	5.94		a* for incandescent light A	19.05	12.05	28.23
	b* for incandescent light A	-2.97	4.20	-1.64		b* for incandescent light A	-12.80	1.19	-9.55
	C* _{ab} for daylight D ₆₅	3.89	10.53	3.20		C* _{ab} for daylight D ₆₅	8.36	9.94	21.94
	h _{ab} (°) for daylight D ₆₅	165.25	131.46	343.66		h _{ab} (°) for daylight D ₆₅	287.68	135.33	334.98
	C* _{ab} for incandescent light A	5.64	4.34	6.16		C* _{ab} for incandescent light A	22.95	12.11	29.80
	h _{ab} (°) for incandescent light A	328.20	75.32	344.57		h _{ab} (°) for incandescent light A	326.10	5.64	341.31
	ΔC* _{ab}	1.75	6.19	2.96		ΔC* _{ab}	14.59	2.17	7.86
	Δh _{ab} (°)	162.95	56.13	0.90		Δh _{ab} (°)	38.43	129.69	6.33
	ΔE* _{ab}	9.43	8.88	2.97		ΔE* _{ab}	17.20	19.98	8.48
2 mm	L* for daylight D ₆₅	63.26	73.33	82.02	7 mm	L* for daylight D ₆₅	20.78	33.86	50.55
	a* for daylight D ₆₅	-3.75	-9.48	6.51		a* for daylight D ₆₅	4.12	-5.24	22.67
	b* for daylight D ₆₅	-1.96	9.60	-2.47		b* for daylight D ₆₅	-7.80	6.43	-10.50
	L* for incandescent light A	62.65	72.89	82.49		L* for incandescent light A	20.81	33.80	52.27
	a* for incandescent light A	9.15	3.02	11.40		a* for incandescent light A	19.99	14.17	31.20
	b* for incandescent light A	-7.44	4.26	-3.53		b* for incandescent light A	-11.95	1.13	-10.36
	C* _{ab} for daylight D ₆₅	4.23	13.49	6.96		C* _{ab} for daylight D ₆₅	8.82	8.29	24.98
	h _{ab} (°) for daylight D ₆₅	207.59	134.64	339.22		h _{ab} (°) for daylight D ₆₅	297.84	129.18	335.15
	C* _{ab} for incandescent light A	11.79	5.22	11.93		C* _{ab} for incandescent light A	23.29	14.21	32.88
	h _{ab} (°) for incandescent light A	320.88	54.67	342.79		h _{ab} (°) for incandescent light A	329.13	4.56	341.63
	ΔC* _{ab}	7.56	8.27	4.97		ΔC* _{ab}	14.47	5.92	7.89
	Δh _{ab} (°)	113.29	79.97	3.57		Δh _{ab} (°)	31.29	124.62	6.48
	ΔE* _{ab}	14.03	13.60	5.03		ΔE* _{ab}	16.40	20.12	8.70
3 mm	L* for daylight D ₆₅	50.65	62.87	74.35	8 mm	L* for daylight D ₆₅	16.33	28.89	45.97
	a* for daylight D ₆₅	-2.53	-10.08	10.05		a* for daylight D ₆₅	5.54	-3.20	25.17
	b* for daylight D ₆₅	-4.80	9.35	-4.29		b* for daylight D ₆₅	-7.33	6.03	-11.47
	L* for incandescent light A	49.99	62.36	75.07		L* for incandescent light A	16.60	29.06	47.94
	a* for incandescent light A	12.73	5.22	16.37		a* for incandescent light A	20.51	16.14	33.72
	b* for incandescent light A	-10.73	3.29	-5.38		b* for incandescent light A	-10.78	1.34	-10.88
	C* _{ab} for daylight D ₆₅	5.43	13.75	10.93		C* _{ab} for daylight D ₆₅	9.19	6.83	27.66
	h _{ab} (°) for daylight D ₆₅	242.21	137.15	336.88		h _{ab} (°) for daylight D ₆₅	307.08	117.95	335.50
	C* _{ab} for incandescent light A	16.65	6.17	17.23		C* _{ab} for incandescent light A	23.17	16.20	35.43
	h _{ab} (°) for incandescent light A	319.87	32.22	341.81		h _{ab} (°) for incandescent light A	332.27	4.75	342.12
	ΔC* _{ab}	11.22	7.58	6.30		ΔC* _{ab}	13.98	9.37	7.77
	Δh _{ab} (°)	77.67	104.93	4.92		Δh _{ab} (°)	25.19	113.21	6.62
	ΔE* _{ab}	16.38	16.46	6.45		ΔE* _{ab}	15.36	19.90	8.79
4 mm	L* for daylight D ₆₅	40.65	53.92	67.45	9 mm	L* for daylight D ₆₅	12.58	24.57	41.84
	a* for daylight D ₆₅	-0.90	-9.66	13.52		a* for daylight D ₆₅	6.79	-1.06	27.37
	b* for daylight D ₆₅	-6.69	8.55	-6.12		b* for daylight D ₆₅	-6.69	5.77	-12.18
	L* for incandescent light A	40.07	53.42	68.42		L* for incandescent light A	13.09	25.00	44.05
	a* for incandescent light A	15.52	7.51	20.83		a* for incandescent light A	20.70	17.92	35.82
	b* for incandescent light A	-12.52	2.30	-7.04		b* for incandescent light A	-9.44	1.76	-11.14
	C* _{ab} for daylight D ₆₅	6.75	12.90	14.84		C* _{ab} for daylight D ₆₅	9.53	5.87	29.96
	h _{ab} (°) for daylight D ₆₅	262.34	138.49	335.65		h _{ab} (°) for daylight D ₆₅	315.43	100.41	336.01
	C* _{ab} for incandescent light A	19.94	7.85	21.99		C* _{ab} for incandescent light A	22.75	18.01	37.51
	h _{ab} (°) for incandescent light A	321.11	17.03	341.33		h _{ab} (°) for incandescent light A	335.49	5.61	342.72
	ΔC* _{ab}	13.19	5.05	7.15		ΔC* _{ab}	13.22	12.14	7.55
	Δh _{ab} (°)	58.77	121.46	5.68		Δh _{ab} (°)	20.06	94.80	6.71
	ΔE* _{ab}	17.43	18.28	7.43		ΔE* _{ab}	14.19	19.40	8.80
5 mm	L* for daylight D ₆₅	32.64	46.22	61.22	10 mm	L* for daylight D ₆₅	9.40	20.79	38.10
	a* for daylight D ₆₅	0.84	-8.59	16.82		a* for daylight D ₆₅	7.84	1.13	29.27
	b* for daylight D ₆₅	-7.67	7.71	-7.81		b* for daylight D ₆₅	-5.96	5.64	-12.65
	L* for incandescent light A	32.22	45.81	62.45		L* for incandescent light A	10.12	21.49	40.54
	a* for incandescent light A	17.59	9.81	24.78		a* for incandescent light A	20.63	19.48	37.53
	b* for incandescent light A	-13.09	1.58	-8.45		b* for incandescent light A	-8.04	2.35	-11.17
	C* _{ab} for daylight D ₆₅	7.72	11.54	18.54		C* _{ab} for daylight D ₆₅	9.85	5.75	31.89
	h _{ab} (°) for daylight D ₆₅	276.25	138.09	335.09		h _{ab} (°) for daylight D ₆₅	322.76	78.67	336.63
	C* _{ab} for incandescent light A	21.93	9.94	26.18		C* _{ab} for incandescent light A	22.14	19.62	39.16
	h _{ab} (°) for incandescent light A	323.34	9.15	341.17		h _{ab} (°) for incandescent light A	338.71	6.88	343.43
	ΔC* _{ab}	14.21	1.61	7.64		ΔC* _{ab}	12.29	13.87	7.27
	Δh _{ab} (°)	47.09	128.94	6.08		Δh _{ab} (°)	15.95	71.79	6.80
	ΔE* _{ab}	17.61	19.40	8.08		ΔE* _{ab}	12.98	18.66	8.74

Path Length		Bl1	Gr1	Pk1
11 mm	L* for daylight D ₆₅	6.74	17.49	34.72
	a* for daylight D ₆₅	8.40	3.28	30.89
	b* for daylight D ₆₅	-5.07	5.60	-12.92
	L* for incandescent light A	7.60	18.46	37.37
	a* for incandescent light A	20.34	20.82	38.88
	b* for incandescent light A	-6.65	3.05	-11.00
	C* _{ab} for daylight D ₆₅	9.81	6.49	33.48
	h _{ab} (°) for daylight D ₆₅	328.89	59.64	337.30
	C* _{ab} for incandescent light A	21.40	21.04	40.41
	h _{ab} (°) for incandescent light A	341.90	8.33	344.20
	ΔC* _{ab}	11.59	14.55	6.92
	Δh _{ab} (°)	13.01	51.31	6.90
	ΔE* _{ab}	12.07	17.75	8.63
12 mm	L* for daylight D ₆₅	4.85	14.58	31.65
	a* for daylight D ₆₅	7.49	5.35	32.23
	b* for daylight D ₆₅	-3.60	5.65	-13.00
	L* for incandescent light A	5.68	15.84	34.50
	a* for incandescent light A	18.79	21.92	39.92
	b* for incandescent light A	-4.88	3.82	-10.66
	C* _{ab} for daylight D ₆₅	8.31	7.78	34.75
	h _{ab} (°) for daylight D ₆₅	334.33	46.56	338.03
	C* _{ab} for incandescent light A	19.41	22.25	41.32
	h _{ab} (°) for incandescent light A	345.44	9.89	345.05
	ΔC* _{ab}	11.10	14.47	6.57
	Δh _{ab} (°)	11.11	36.68	7.02
	ΔE* _{ab}	11.40	16.72	8.53
13 mm	L* for daylight D ₆₅	3.53	12.03	28.86
	a* for daylight D ₆₅	6.53	7.29	33.32
	b* for daylight D ₆₅	-2.41	5.76	-12.91
	L* for incandescent light A	4.30	13.55	31.90
	a* for incandescent light A	16.04	22.79	40.66
	b* for incandescent light A	-3.07	4.65	-10.18
	C* _{ab} for daylight D ₆₅	6.96	9.29	35.73
	h _{ab} (°) for daylight D ₆₅	339.74	38.31	338.82
	C* _{ab} for incandescent light A	16.33	23.26	41.92
	h _{ab} (°) for incandescent light A	349.16	11.53	345.94
	ΔC* _{ab}	9.37	13.97	6.18
	Δh _{ab} (°)	9.42	26.78	7.12
	ΔE* _{ab}	9.56	15.61	8.40

L*	lightness parameter in the three-dimensional CIELAB color space
a*, b*	rectangular parameters in the three-dimensional CIELAB color space
C* _{ab} for daylight D ₆₅	chroma (saturation) for daylight D ₆₅
h _{ab} (°) for daylight D ₆₅	hue angle for daylight D ₆₅
C* _{ab} for incandescent light A	chroma (saturation) for incandescent light A
h _{ab} (°) for incandescent light A	hue angle for incandescent light A
Δh _{ab} (°)	hue angle difference between daylight and incandescent light
ΔC* _{ab}	chroma difference between daylight and incandescent light
ΔE* _{ab}	color difference between daylight and incandescent light in the three-dimensional CIELAB color space

without an accurate quantitative calculation, and this behavior is expected to vary between different gem materials.

An interesting phenomenon was observed in the color difference vs. path length plots of Bl1 and Gr1. When the stone becomes darker with increasing path length, a small bump forms instead of a smooth curved line (figure 19, left column). Presently, we cannot offer an explanation for this unusual behavior.

Color Difference ΔE*_{ab} vs. Hue Angle Difference Δh_{ab} Plots, and the Problem of “Color Change.” Color difference vs. hue angle difference plots reveal that Bl1 and Gr1 show a larger color difference ΔE*_{ab} and hue angle difference Δh_{ab} than Pk1 at nearly all path lengths (figure 20).

Liu et al. (1994, 1999a) suggested that a stone should have a hue angle difference Δh_{ab} larger than 20° and a chroma difference ΔC*_{ab} higher than 5 to be considered a color-change stone. Schmetzer et al. (2009) proposed three different sets of criteria that could be used to decide whether to describe a stone as having a “color change.” The first set of criteria suggests that a stone should have a hue angle difference Δh_{ab} larger than 60° or a color difference ΔE*_{ab} larger than 9. The second and third set of criteria are shown graphically in figures 20 and 21, respectively, and offer a distinction between “color change” and “color variation” depending on where the stone plots in a specific region of the ΔE*_{ab} vs. Δh_{ab} space.

To facilitate discussion of color change and its relationship to path length in these three stones, the color of Bl1, Gr1, and Pk1 under daylight-equivalent light and incandescent light was quantitatively reproduced for path lengths from 1 mm to 13 mm by converting CIE L*, a*, and b* color space coordinates into color swatches using Adobe Photoshop (figure 22).

According to the classification of Liu et al. (1994, 1999a), Bl1 can be considered to have a color change when the path length of light passing through the stone is between 3 and 9 mm. Likewise, Gr1 is a color-change garnet when the path length is between 2 and 13 mm. Because Pk1’s hue angle difference Δh_{ab} is never larger than 20°, it cannot be considered a color-change stone according to this classification.

According to the first classification of Schmetzer et al. (2009) described above, Bl1 is a color-change stone when path length is between 1 and 13 mm, Gr1 is a color-change stone when path length is between 2 and 13 mm, and Pk1 is never a color-change

garnet because its ΔE^*_{ab} is never larger than 9 and its Δh_{ab} is never larger than 60° . According to the second classification scheme of Schmetzer et al. (2009), Bl1 is a color-change stone when path length is between 1 and 13 mm, as are Gr1 when path length is between 1 and 13 mm and Pk1 when path length is between 4 and 13 mm (again, see figure 20). According to the third classification scheme of Schmetzer et al. (2009), Bl1 is a color-change stone at path lengths between 1 and 13 mm, as is Gr1 at path lengths between 1 and 13 mm, and Pk1 is never a color-change garnet (figure 21).

Considering the ΔE^*_{ab} vs. Δh_{ab} plots used by Schmetzer et al. (2009) as criteria, it makes sense intuitively that stones with low ΔE^*_{ab} and Δh_{ab} values do not possess a color change. Likewise, stones with high ΔE^*_{ab} but very low Δh_{ab} should probably not be described as “color-change”—even though the saturation and/or lightness may change between daylight-equivalent and incandescent lighting, there will be no significant change in hue, which is likely the most important factor. Nor do samples with large Δh_{ab} but very small ΔE^*_{ab} values qualify as color-change stones, because their saturation is too low for color differences to be readily observed. It should be pointed out that there is no unique solution to the problem of classifying color-change stones based on their CIELAB color coordinates, as the entire concept of “color change” is inherently subjective. A more objective boundary for color-change stones might be achieved through a comprehensive survey of gemologists, jewelers, collectors, and gem enthusiasts. But

TABLE 3. Proportions of the round brilliant cut garnet used to demonstrate the relationship between carat weight and path length.

Crown angle (°)	35.00
Pavilion angle (°)	38.50
Total height (%)	59.35
Crown height (%)	15.06
Pavilion height (%)	39.79
Table (%)	57.02
Girdle height bezel (%)	4.50
Star angle (°)	20.75
Upper girdle angle (°)	41.10
Lower girdle angle (°)	39.56

even the most comprehensive survey cannot be expected to provide an absolute classification scheme for color-change gems.

The Relationship Between Carat Weight and Actual Path Length in a Standard Round Brilliant. To relate the path lengths used in our color calculations above to the size of faceted stones, we report here the results of calculations, using DiamCalc software, that show the relationship between carat weight and actual path length for a 57-facet round brilliant garnet. The stone has an RI of 1.750 and an SG of 3.875; its proportions are listed in table 3. The path length represents a ray of light entering the garnet at approxi-

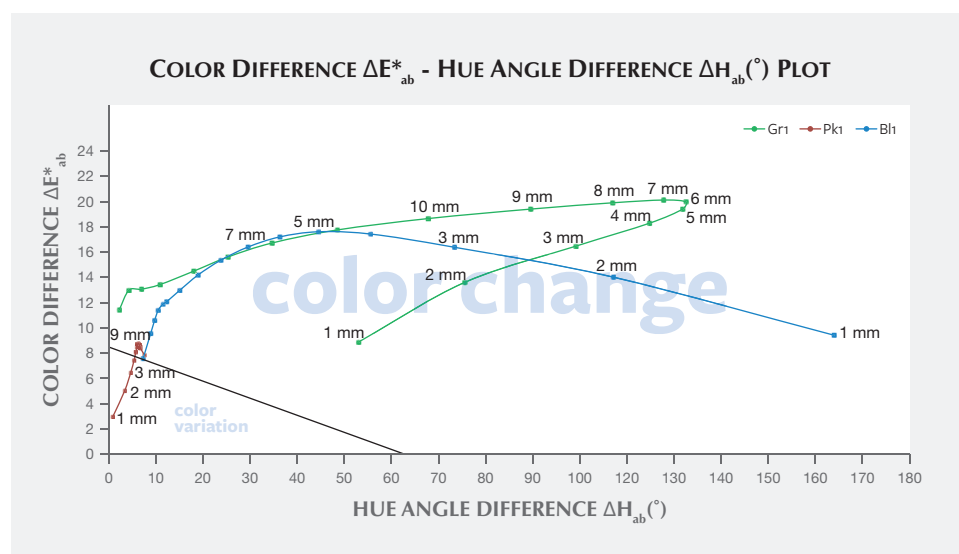


Figure 20. Color difference ΔE^*_{ab} vs. hue angle difference Δh_{ab} plot of three garnets with different path lengths (modified after Schmetzer et al., 2009).

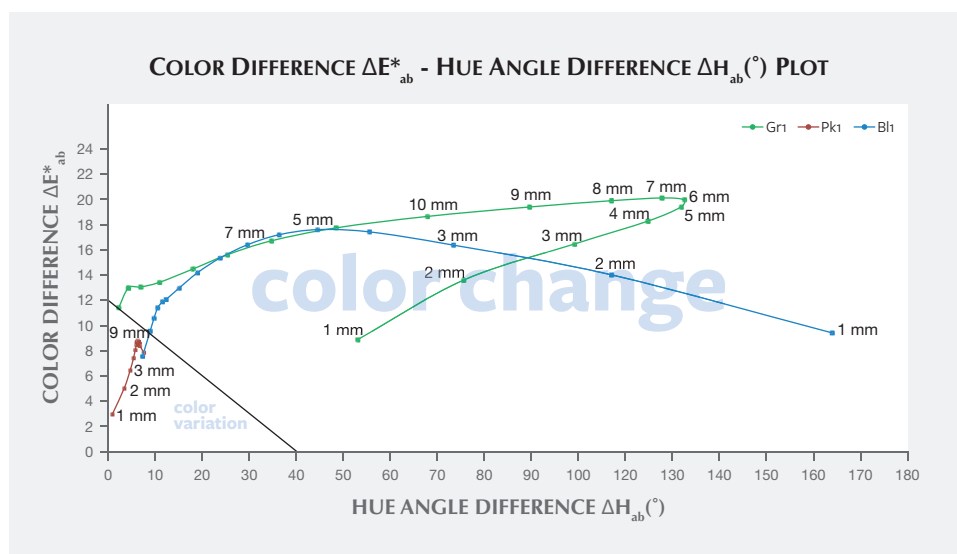
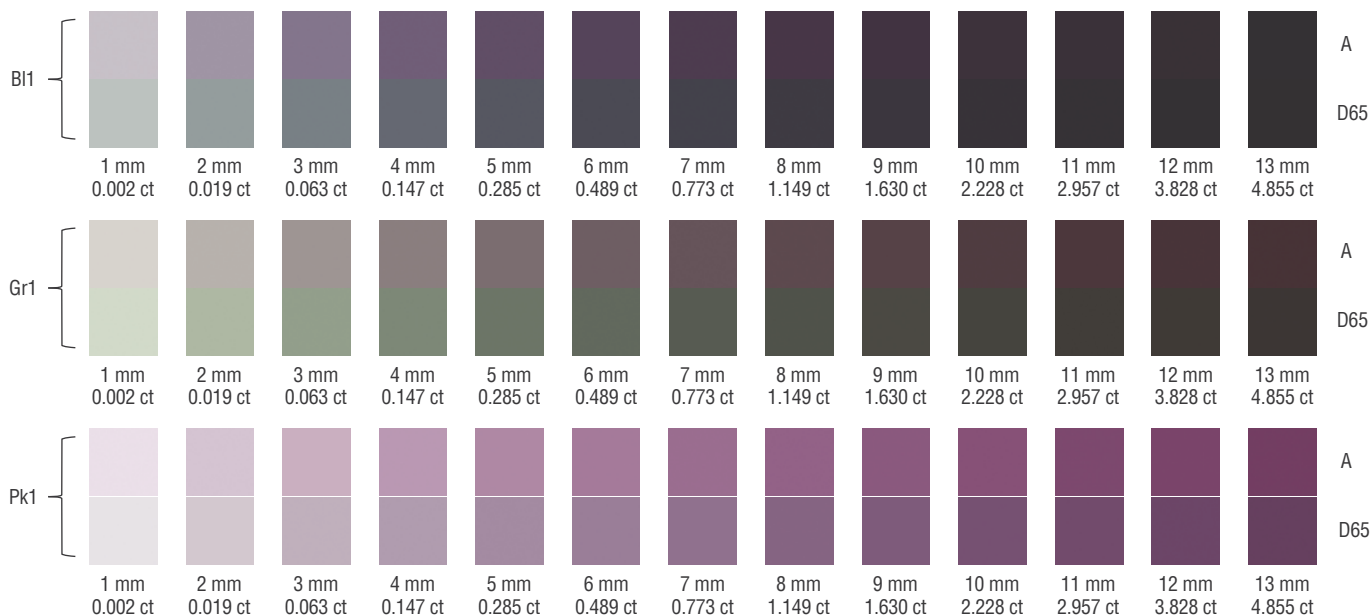


Figure 21. Color difference ΔE^*_{ab} vs. hue angle difference ΔH_{ab} plot of three garnets with different path lengths (modified after Schmetzer et al., 2009).

mately 70° to the plane of the girdle (from over the shoulder of the observer). The light passes through the middle of a bezel facet, strikes the middle of a pavilion main facet, and is reflected to the opposing pavilion main facet before exiting through the table to the eye of the observer directly overhead (red line in figure 23). The carat weight of each path length from 1 to 13 mm was calculated and is reported in

figure 22. This calculation is only for round brilliants of the specific proportions presented in table 3. The path length will vary with the way the stone is cut. The concentration, distribution, and orientation of the inclusions will influence how the light passes through and is absorbed into the stone. This factor has not been corrected for individual stones in this study.

Figure 22. The color of three stones under daylight-equivalent light (D65) and incandescent light (A) is quantitatively reproduced by converting CIE L^* , a^* , b^* color space coordinates into color swatches using Adobe Photoshop. The colors of Bl1, Gr1, and Pk1 are shown at different path lengths and carat weights. For each sample, the two rows represent the color under incandescent lighting (top), and daylight-equivalent light (bottom).



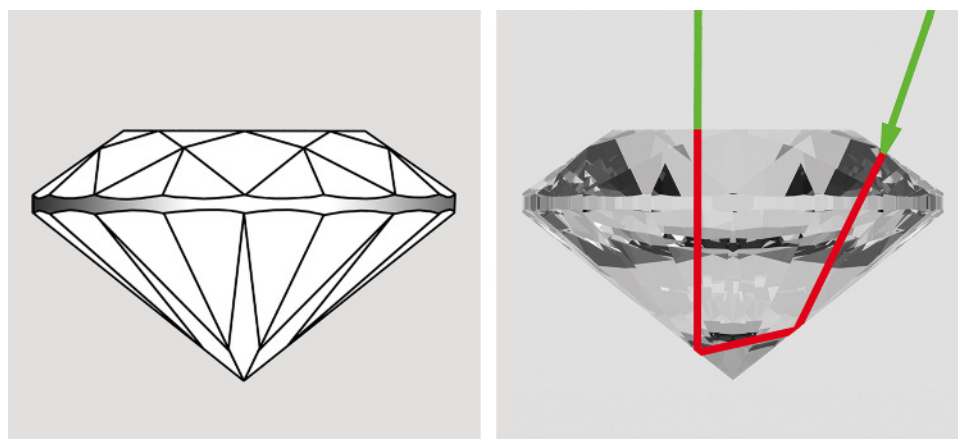


Figure 23. Diagram of the round brilliant garnet (left) and the calculated path length inside the stone (right, red line). Photo by Al Gilbertson.

CONCLUSIONS

What sets this type of pink pyrope garnet apart from other color-change pyrope-spessartine garnets is the somewhat lower concentration of vanadium and chromium and also the much higher pyrope component ($\text{Mg}_3\text{Al}_2\text{Si}_3\text{O}_{12}$). From the colorimetric analysis of three different samples, we have the following thoughts.

The Usambara effect and color change are two manifestations of the phenomenon of having two distinct transmission windows in the visible spectrum. This study quantitatively described the interplay between color change and the Usambara effect (Schmetzer et al., 2013).

To make this comparison between the Usambara effect and color change, a reflection loss correction method was developed. This method allowed us to accurately manipulate the UV-Vis spectra to calculate color under different lighting conditions for various path lengths.

As path length increases, the difference in color between incandescent and daylight-equivalent lighting increases at first as chroma (saturation), chroma difference, or hue angle difference increases. The color difference then decreases as chroma, chroma difference, or hue angle difference decreases. This latter effect occurs because one of the transmission windows is preferentially “closed” in the thicker portions of the stone.

By this reasoning, there is one path length that should show the greatest difference in color between incandescent and daylight-equivalent lighting, another with the greatest hue angle variation, and still another with the greatest saturation variation. While this path length may not be the same in all cases, there should be a range of path lengths that show the best color change. Below or above this range, the saturation is too low or the hue angle change or saturation change is too slight to produce an observable color change.

ABOUT THE AUTHORS

Mr. Sun is a staff gemologist, Dr. Palke is a postdoctoral research associate, and Mr. Renfro is the analytical manager of the gem identification department and analytical microscopist in the inclusion research department, at GIA in Carlsbad, California.

ACKNOWLEDGMENTS

The authors thank Todd Wacks from Todd's Gems, Jason Doubrava from Jason Doubrava Gems & Minerals, Meg Berry from Megagem and Jeff Hapeman from Earth's Treasury, for providing samples for chemical analyses and inclusion photomicrography. Assistance from Jonathan Muyal in polishing the garnet wafers and

taking photomicrographs of inclusions is greatly appreciated. The authors thank two anonymous reviewers for their constructive comments and criticism, which helped to improve this article. The authors thank Al Gilbertson for using DiamCalc software to calculate the relationship between path length and carat weight; Dino DeGhionno, Shane McClure, Mike Breeding, David Nelson, Troy Ardon, Yun Luo, and Tao Hsu for many helpful mineralogical and colorimetric discussions. Virginia Schwartz, Philip York, Amy Cooper, Heidi Breitzmann, Philip Owens, Claire Ito, Rebecca Tsang, Najmeh Anjomani, Johna Lippert, and Jenni Rieger provided invaluable assistance in gemological testing and discussions. The photos of the samples in table 1 are by Robison McMurtry.

REFERENCES

- Amthauer G. (1975) Kristallchemie und Farbe chromhaltiger Granate. *Neues Jahrbuch für Mineralogie Abhandlungen*, Vol. 126, No. 2, pp. 158–186 [in German].
- Björn L. O. (2002) *Photobiology: The Science of Light and Life*. Kluwer Academic Publishers, Dordrecht, Netherlands.
- Carstens H. (1973) The red-green change in chromium-bearing garnets. *Contributions to Mineralogy and Petrology*, Vol. 41, pp. 273–276, <http://dx.doi.org/10.1007/BF00371036>
- CIE Commission Internationale de l'Éclairage (2004) CIE 15: Technical Report: Colorimetry. 3rd edition
- Crowningshield R. (1970) A rare alexandrite garnet from Tanzania. *G&G*, Vol. 13, No. 6, pp. 174–177.
- Geiger C.A., Stahl A., Rossman G.R. (2000) Single-crystal IR- and UV/VIS-spectroscopic measurements on transition-metal bearing pyrope: the incorporation of hydroxide in garnet. *European Journal of Mineralogy*, Vol. 12, No. 2, pp. 259–271, <http://dx.doi.org/10.1127/0935-1221/2000/0001-0259>
- Gübelin E.J., Koivula J.I. (2005) *Photoatlas of Inclusions in Gemstones*, Vol. 2, Opinio, Basel, Switzerland, pp. 430–469.
- Halvorsen A. (2006) The Usambara effect and its interaction with other color change phenomena. *Journal of Gemmology*, Vol. 30, No. 1/2, pp. 1–21.
- Halvorsen A., Jensen B.B. (1997) A new color change effect. *Journal of Gemmology*, Vol. 25, No. 5, pp. 325–330.
- Hysingjord J. (1971) A gem garnet from the island of Otterøy. *Journal of Gemmology*, Vol. 12, No. 7, pp. 296–299.
- Jobbins E.A., Saul J.M., Tresham A.E., Young B.R. (1975) Blue color-change gem garnet from East Africa. *Journal of Gemmology*, Vol. 14, No. 5, pp. 201–208.
- Johnson M.L., Koivula J.I., Eds. (1998) Gem News: Color change pyrope-spessartine garnet, also from Madagascar. *G&G*, Vol. 34, No. 3, pp. 222–223.
- Koivula J.I. (1984) The first-order red compensator: an effective gemological tool. *G&G*, Vol. 20, No. 2, pp. 101–105, <http://dx.doi.org/10.5741/GEMS.20.2.101>
- (2000) *The Microworld of Diamonds*. Gemworld International. Northbrook, IL.
- Krzemnicki M.S., Hänni H.A., Reusser E. (2001) Color-change garnets from Madagascar: comparison of colorimetric with chemical data. *Journal of Gemmology*, Vol. 27, No. 7, pp. 395–408.
- Liu Y., Shigley J.E., Fritsch E., Hemphill S. (1994) The “alexandrite effect” in gemstones. *Color Research and Application*, Vol. 19, No. 3, pp. 186–191.
- Liu Y., Shigley J.E., Fritsch E., Hemphill S. (1999a) A colorimetric study of the alexandrite effect in gemstones. *Journal of Gemmology*, Vol. 26, No. 6, pp. 371–385.
- Liu Y., Shigley J.E., Halvorsen A. (1999b) Colour hue change of a gem tourmaline from the Umba Valley, Tanzania. *Journal of Gemmology*, Vol. 26, No. 6, pp. 386–396.
- Locock A.J. (2008) An Excel spreadsheet to recast analyses of garnet into end-member components, and a synopsis of the crystal chemistry of natural silicate garnets. *Computers & Geosciences*, Vol. 34, pp. 1769–1780, <http://dx.doi.org/10.1016/j.cageo.2007.12.013>
- Manson D.V., Stockton C.M. (1984) Pyrope-spessartine garnets with unusual color behavior. *G&G*, Vol. 20, No. 4, pp. 200–207, <http://dx.doi.org/10.5741/GEMS.20.4.200>
- Moore R.K., White W.B. (1972) Electronic spectra of transition metal ions in silicate garnets. *Canadian Mineralogist*, Vol. 11, pp. 791–811.
- Pay D. (2015) Gem News International: Color-change garnets from Tanzania. *G&G*, Vol. 51, No. 1, pp. 88–89.
- Renfro N. (2015a) Digital photomicrography for gemologists. *G&G*, Vol. 51, No. 2, pp. 144–159, <http://dx.doi.org/10.5741/GEMS.51.2.144>
- (2015b) The application of differential interference contrast microscopy to gemmology. *Journal of Gemmology*, Vol. 34, No. 7, pp. 616–620.
- Schmetzer K., Ottemann J. (1979) Kristallchemie und Farbe Vanadium-haltiger Granate. *Neues Jahrbuch für Mineralogie Abhandlungen*, Vol. 136, No. 2, pp. 146–168 [in German].
- Schmetzer K., Bernhardt H.-J., Bosshart G., Hainschwang T. (2009) Color-change garnets from Madagascar: variation of chemical, spectroscopic and colorimetric properties. *Journal of Gemmology*, Vol. 31, No. 5–8, pp. 235–282.
- Schmetzer K., Bernhardt H.-J., Balmer W.A., Hainschwang T. (2013) Synthetic alexandrites grown by the HOC method in Russia: internal features related to the growth technique and colorimetric investigation. *Journal of Gemmology*, Vol. 33, No. 5–6, pp. 113–129.
- Stockton C.M. (1988) Pastel pyropes. *G&G*, Vol. 24, No. 2, pp. 104–106, <http://dx.doi.org/10.5741/GEMS.24.2.104>
- Stockton C.M., Manson D.V. (1985) A proposed new classification for gem-quality garnets. *G&G*, Vol. 21, No. 4, pp. 205–218, <http://dx.doi.org/10.5741/GEMS.21.4.205>

For More on "Color-Change" Pyrope Garnet

Learn More About "Color-Change" Pyrope Garnet: G&G's exclusive interviews and photo galleries looks at the history, market forecast, and custom jewelry design for this fascinating material spotlighted at the 2015 Tucson gem shows.



Visit <http://www.gia.edu/gems-gemmology/spring-2015-gemnews-color-change-garnets-tanzania>, or scan the QR code on the right.